

1 **Distinctive aerosol-cloud-precipitation interactions in marine boundary layer clouds from the**  
2 **ACE-ENA and SOCRATES aircraft field campaigns**

3  
4 Xiaojian Zheng<sup>1,a</sup>, Xiquan Dong<sup>1</sup>, Baike Xi<sup>1</sup>, Timothy Logan<sup>2</sup> and Yuan Wang<sup>3</sup>

5  
6 <sup>1</sup>Department of Hydrology and Atmospheric Sciences, University of Arizona, Tucson, AZ, USA

7 <sup>2</sup>Department of Atmospheric Sciences, Texas A&M University, College Station, TX, USA

8 <sup>3</sup>Department of Earth System Sciences, Stanford University, Stanford, CA, USA

9 <sup>a</sup>Now at: Environmental Science Division, Argonne National Laboratory, Lemont, IL, USA

10  
11 **Correspondence:** Xiquan Dong ([xdong@arizona.edu](mailto:xdong@arizona.edu))

12  
13 **Abstract.** The aerosol-cloud-precipitation interactions within the cloud-topped Marine Boundary Layer  
14 (MBL) are being examined using aircraft in-situ measurements from Aerosol and Cloud Experiments in  
15 the Eastern North Atlantic (ACE-ENA) and Southern Ocean Clouds Radiation Aerosol Transport  
16 Experimental Study (SOCRATES) field campaigns. SOCRATES clouds have a larger number and  
17 smaller cloud droplets ( $148.3 \text{ cm}^{-3}$  and  $8.0 \text{ }\mu\text{m}$ ) compared to ACE-ENA summertime ( $89.4 \text{ cm}^{-3}$  and  $9.0$   
18  $\mu\text{m}$ ) and wintertime clouds ( $70.6 \text{ cm}^{-3}$  and  $9.8 \text{ }\mu\text{m}$ ). The ACE-ENA clouds, especially in wintertime,  
19 exhibit stronger drizzle formation and growth due to enhanced collision-coalescence, attributed to the  
20 relatively cleaner environment and deeper cloud layer. Furthermore, the Aerosol-Cloud Interaction (ACI)  
21 indices from the two aircraft field campaigns suggest distinct sensitivities, indicating the cloud  
22 microphysical responses to aerosols reside in different regimes. Aerosols during ACE-ENA winter are  
23 more likely to be activated into cloud droplets under sufficient water availability and strong turbulence,  
24 given the aerosol-limited regime. The enriched aerosol loading during ACE-ENA summer and  
25 SOCRATES generally leads to smaller cloud droplets competing for available water vapor and exhibiting

26 a stronger ACI in the water-vapor-limit regime. Notably, the precipitation susceptibilities are more  
27 pronounced during the ACE-ENA than during the SOCRATES campaigns. The in-cloud drizzle  
28 evolutions significantly alter sub-cloud cloud condensation nuclei (CCN) budgets through the  
29 coalescence-scavenging effect, and in turn, impact the ACI assessments. The results of this study can  
30 enhance the understanding and aid in future model simulation and assessment of the aerosol-cloud  
31 interaction.

32

33

## 34 **1. Introduction**

35 Marine boundary layer (MBL) clouds substantially impact the Earth's climate system (Dong and  
36 Minnis, 2022). Sustained by large-scale subsidence and cloud-top longwave radiative cooling, MBL  
37 clouds, typically located beneath the temperature inversion at the MBL top, persistently reflect the  
38 incoming solar radiation and modulate the radiative balance (Lilly, 1968; Albrecht et al., 1995; Wood et  
39 al., 2015; Dong et al., 2023). The climatic significance of MBL cloud radiative effects, which remains  
40 largely uncertain (IPCC, 2022), is closely linked to cloud microphysical properties that are substantially  
41 influenced by surrounding aerosol conditions (Chen et al., 2014; Feingold and McComiskey, 2016).  
42 Observational evidence demonstrates that cloud microphysical responses to aerosols, defined as the  
43 aerosol-cloud interaction (ACI), can be typically viewed as decreased cloud droplet effective radii ( $r_c$ )  
44 and increased number concentrations ( $N_c$ ) with more aerosol intrusion under conditions of comparable  
45 cloud water content (Feingold and McComiskey, 2016). The ACIs have been extensively investigated  
46 by different observational platforms, such as aircraft (Hill et al., 2009; Diamond et al., 2018; Gupta et  
47 al., 2022), ground-based and satellite observations (Painemal et al., 2020; Zhang et al., 2022; Zheng et  
48 al., 2022a), and model simulations (Wang et al., 2020; Christensen et al., 2023) over different maritime  
49 regions like the southeast Pacific (Painemal and Zuidema, 2011), northeast Pacific (Braun et al., 2018),  
50 southeast Atlantic (Gupta et al., 2022), and eastern North Atlantic (Zheng et al., 2022a).

51           Furthermore, more and smaller cloud droplets not only extend cloud longevity and spatial  
52 coverage but also modulate the precipitation processes, reflecting the cloud adjustments to aerosol  
53 disturbances (Albrecht, 1989; Bellouin et al., 2020). Precipitation, particularly in the form of drizzle, is  
54 common in MBL clouds (Wood et al., 2015; Wu et al., 2020), and the turbulence forced by stratocumulus  
55 cloud-top radiative cooling can increase the cloud liquid water path and contribute to drizzle production  
56 (Ghate et al., 2019, 2021). The drizzle formation and growth processes are deeply entwined with the  
57 MBL aerosols and dynamics. Aerosols have been found to suppress the precipitation frequency and  
58 strength by constantly buffering cloud droplet number concentrations via activation, hence increasing  
59 cloud precipitation susceptibility (Feingold and Seibert, 2009; Lu et al., 2009; Sorooshian et al., 2009;  
60 Duong et al., 2011). Furthermore, the assessments of precipitation susceptibility are examined to be under  
61 the influences of methodology (Terai et al., 2012), cloud morphology (Sorooshian et al., 2009; Jung et  
62 al., 2016), ambient aerosol concentrations (Duong et al., 2011; Jung et al., 2016; Gupta et al., 2022), and  
63 cloud thickness (Terai et al., 2012; Jung et al., 2016; Gupta et al., 2022). The in-cloud turbulence and  
64 wind shear can effectively enhance collision-coalescence efficiency, stimulating drizzle formation and  
65 growth, and consequently leading to enhanced precipitation (Chen et al., 2011; Wu et al., 2017). Cloud-  
66 top entrainment of dryer and warmer air can potentially deplete small cloud droplets and shrink large  
67 droplets via evaporation, thereby impacting cloud top microphysical processes depending on the  
68 homogeneous or inhomogeneous mixing regimes (Lehmann et al., 2009; Jia et al., 2019).

69           Conversely, precipitation has been shown to exert a substantial influence on the MBL aerosol and  
70 cloud condensation nuclei (CCN) budget through the coalescence-scavenging effect. The coalescence-  
71 scavenging refers to the process in which cloud or drizzle droplets, containing aerosol particles inside,  
72 merge with each other. Upon the collision-coalescence of cloud droplets, the dissolved aerosol masses  
73 within the cloud droplets also collide and merge into a larger aerosol core, leading to larger aerosol  
74 particles upon droplet evaporation. The sub-cloud aerosols are then replenished into the cloud layer,  
75 experiencing growth within the cloud through cloud and drizzle droplet collision-coalescence and

76 subsequently falling and evaporating outside the cloud again. Eventually, the residual aerosols  
77 undergoing this cloud-processing cycle will gradually decrease in number concentration and increase in  
78 size (Flossmann et al., 1985; Feingold et al., 1996; Hudson and Noble, 2020; Hoffmann and Feingold,  
79 2023). In addition, the drizzle drops, once falling out of the cloud base, can result in net reductions in  
80 sub-cloud aerosols and CCN budgets also via the precipitation scavenging processes (Wood, 2006;  
81 Zheng et al., 2022b). Quantitative estimates of these effects remain ambiguous and inconclusive, which  
82 are subject to multiple factors such as aerosol physicochemical characteristics, cloud morphology, and  
83 MBL dynamics and thermodynamics conditions (Sorooshian et al., 2009; Duong et al., 2011; Diamond  
84 et al., 2018; Brunke et al., 2022). Thus, more studies on the aforementioned processes regarding MBL  
85 aerosols and clouds over different maritime regions are warranted to pursue an in-depth understanding  
86 of aerosol-cloud-precipitation interactions (ACPIs).

87         The Eastern North Atlantic (ENA) stands as a desirable region for exploring MBL clouds in the  
88 mid-latitude, with Graciosa Island in the Azores (39.09°N, 28.03°W) representing a focal point for such  
89 studies. Located between the mid-latitude and subtropical climate zones, Graciosa is subject to the  
90 meteorological influence of both the Icelandic Low and the Azores High, and the influence of aerosols  
91 ranging from pristine marine air masses to those heavily influenced by continental emissions from North  
92 America and Northern Europe (Logan et al., 2014; Wood et al., 2015; Wang et al., 2020). Addressing  
93 the need for sustained research into the MBL clouds, the recent Aerosol and Cloud Experiments in the  
94 Eastern North Atlantic (ACE-ENA) aircraft campaign (J. Wang et al., 2022) were conducted in the  
95 summer (June and July) 2017 (ACE-ENA Sum) and winter (January and February) 2018 (ACE-ENA  
96 Win). During these two intensive operation periods (IOPs) of ACE-ENA, the research aircraft accrued  
97 abundant in-situ measurements of aerosols, clouds, and drizzle properties, providing invaluable resources  
98 for studying the ACI and ACPI processes. During the summer, the Azores is located at the eastern part  
99 of the high-pressure system, while during the winter, the center of the Azores high shifts to the eastern  
100 Atlantic and is primarily located directly over the Azores (Mechem et al., 2018; J. Wang et al., 2022).

101 Furthermore, both summer and winter IOPs of ACE-ENA featured anomalously strong high-pressure  
102 systems, compared to the 20-year climatology, as shown in Figure S1. This meteorological pattern is  
103 favorable to the prevailing and persistent stratocumulus clouds observed during the ACE-ENA,  
104 especially for the winter IOP, where the enhanced large-scale subsidence would lead to stronger and  
105 sharper temperature inversion above the stratocumulus-topped MBL (Rémillard and Tselioudis, 2015;  
106 Jensen et al., 2021; Marcovecchio et al., 2022). The ACE-ENA summer IOP is characterized by  
107 anomalously low MBL heights and substantial MBL decoupling (Miller et al., 2021; J. Wang et al., 2022).  
108 The winter IOP was under the frequent impacts of the mid-latitude systems and prevalently featured  
109 precipitation-generated cold pools, where evaporative cooling alters the thermodynamical structure of  
110 the MBL, sustains and enhances turbulence mixing, hence contributes to dynamical perturbations that  
111 can influence the behavior of the MBL (Terai and Wood, 2013; Zuidema et al., 2017; Jensen et al., 2021;  
112 J. Wang et al., 2022; Smalley et al., 2024). In recent years, many observational studies based on ACE-  
113 ENA data have focused on the seasonal contrasts of the aerosol distributions and sources (Y. Wang et  
114 al., 2021b; Zawadowicz et al., 2021), the cloud and drizzle microphysics vertical distributions (Wu et al.,  
115 2020a; Zheng et al., 2022b), as well as the impacts of MBL conditions on the cloud structure and  
116 morphology (Jensen et al., 2021). However, they seldom analyze the comprehensive interactions between  
117 aerosol, clouds and precipitation.

118 Over the Southern Ocean (SO), the Southern Ocean Clouds Radiation Aerosol Transport  
119 Experimental Study (SOCRATES) field campaign (McFarquhar et al., 2021) was conducted during the  
120 austral summer (January and February 2018), which marks another valuable piece of the MBL cloud  
121 research. The SO, being one of the cloudiest regions globally, is predominantly influenced by naturally  
122 produced aerosols originating from oceanic sources due to its remoteness, where the anthropogenic and  
123 biomass burning aerosols exert minimal influence over the region (McCoy et al., 2021; Sanchez et al.,  
124 2021; Twohy et al., 2021; Zhang et al., 2023). The aerosol budget in this region is primarily shaped by  
125 biological aerosols, which nucleate from the oxidation products of dimethyl sulfide (DMS) emissions, as

126 well as by sea spray aerosols. Hence, the SO provides an unparalleled natural laboratory for discerning  
127 the influence of these natural aerosol emissions on the MBL clouds under a pre-industrial natural  
128 environment. The summertime SO region, particularly near the SOCRATES focus area, is characterized  
129 by more frequently closed-cell mesoscale cellular convection structures (Danker et al., 2022; Lang et al.,  
130 2022). Furthermore, the MBL clouds over the SO predominantly consist of supercooled liquid water  
131 droplets, which coexist with mixed- and ice-phase processes (Y. Wang et al., 2021a; Xi et al., 2022),  
132 while the precipitation phases are examined to be primarily dominated by liquid hydrometeors (Tansey  
133 et al., 2022; Kang et al., 2024). The in-situ measurements collected from SOCRATES have cultivated  
134 numerous studies on aerosols, clouds, and precipitation over the SO using both in-situ measurements and  
135 model simulations (McCoy et al., 2020; Altas et al., 2021; D'Alessandro et al., 2021), and provides an  
136 opportunity to study the liquid cloud processes under a colder nature. As shown in Figure S1c,  
137 compositely speaking, the SOCRATES cloud cases used in this study are located ahead of the  
138 anomalously strong thermal ridge and behind the thermal trough, providing a set up favorable to the  
139 closed cellular MBL cloud structures (McCoy et al., 2017; Lang et al., 2022). The region of selected  
140 SOCRATES cloud cases crosses a larger latitudinal zone and is under more consistent influence of mid-  
141 latitude cyclone systems than the ACE-ENA during the summer IOP, the cloud sampling periods used  
142 in this study majority reside in the closed-cell MBL stratocumulus decks.

143         The cloud cases selected from the ACE-ENA and SOCRATES share similar cloud morphology  
144 (stratocumulus) while experiencing different aerosol sources and meteorological conditions. Using a  
145 synergistic approach to compare data from these different field campaigns can provide valuable insights  
146 to the community regarding the dominant physical processes of the interactions between aerosols, clouds,  
147 and precipitation under the influence of different MBL dynamic and thermodynamic conditions. This  
148 study targets the similarities and differences in the MBL aerosol, cloud, and drizzle properties, their  
149 distribution and evolution, and more appealingly, the ACIs and ACPIs between the two campaigns. The  
150 data and methods used in this study are introduced in section 2. The aerosol and CCN properties in the

151 above- and sub-cloud regimes, as well as the vertical distributions of MBL cloud and drizzle properties,  
152 are examined in section 3. The ACI, precipitation susceptibility and drizzle impacts on the sub-cloud  
153 aerosols and CCN (ACPI) are discussed in section 4. Finally, the findings are summarized, and the  
154 importance of this study is discussed in section 5.

155

## 156 **2. Data and methods**

### 157 **2.1 Cloud and drizzle properties**

158 The in-situ measurements of MBL cloud properties are temporally synchronized to 1 Hz  
159 resolution, corresponding to approximately 100 m (5 m) of horizontal (vertical) sampling. The sampling  
160 locations of the selected cases are indicated by the white dots in Figure S1. The Fast Cloud Droplet Probe  
161 (FCDP) onboard the aircraft during ACE-ENA can detect droplets with diameter ( $D_p$ ) ranging from 1.5  
162  $\mu\text{m}$  to 50  $\mu\text{m}$ , with the size bins of the probe between 1 and 3  $\mu\text{m}$  (Glienke and Mei, 2020). While the  
163 SOCRATES used a similar CDP to measure droplets from 2  $\mu\text{m}$  to 50  $\mu\text{m}$  at a 2  $\mu\text{m}$  probe size bin width.  
164 Both ACE-ENA and SOCRATES leverage the Two-Dimensional Stereo Particle Imaging Probe (2DS)  
165 to discern droplets with diameters from 5  $\mu\text{m}$  to 1280  $\mu\text{m}$  (Lawson et al., 2006; Glienke and Mei, 2019).  
166 The 2DS in-situ measurements will be used as additional screening to eliminate the ice particles with  
167 diameters larger than 200  $\mu\text{m}$ . Moreover, the University of Washington Ice–Liquid Discriminator  
168 product, which is a Machine-learning-based single-particle phase classification of the 2DS images (Atlas  
169 et al., 2021), is used to identify small ice crystals when available. Through these three datasets, we can  
170 tease out the ice-dominated period to the utmost extent and focus on the liquid cloud processes and ACI  
171 during the SOCRATES (Wang et al., 2021).

172 Although these in-situ measurements can provide “ground-truth” datasets, their uncertainties  
173 must be properly analyzed and data quality must be controlled before being applied to scientific studies.  
174 The uncertainties of FCDP in sizing and concentration are approximately 30% and 20%, respectively  
175 (Baumgardner et al., 2017). Considering the significant uncertainty in the concentration of smaller

176 particles from a photodiode probe such as 2DS (Baumgardner & Korolev, 1997; Wang et al., 2021), a  
 177 diameter of 40  $\mu\text{m}$  is used as the demarcation line between cloud droplets and drizzle drops (Wood et al.,  
 178 2005). Then droplet number concentrations in the overlapping size bin between FCDP and 2DS are  
 179 redistributed assuming a gamma distribution, thereby a complete size spectrum of cloud and drizzle can  
 180 be merged from FCDP and 2DS measurements. Hence, the cloud and drizzle microphysical properties  
 181 can be calculated.

182 The cloud droplet number concentration ( $N_c$ ) is given by:

$$183 \quad N_c = \int_2^{40} n(D_p) dD_p, \quad (1)$$

184 The cloud droplet effective radius ( $r_c$ , Hansen and Travis, 1974) is given by:

$$185 \quad r_c = \frac{\int_2^{40} r_p^3 n(D_p) dD_p}{\int_2^{40} r_p^2 n(D_p) dD_p}, \quad (2)$$

186 The cloud liquid water content ( $LWC_c$ ) can be calculated by:

$$187 \quad LWC_c = \frac{4}{3} \pi \rho_w \int_2^{40} D^3 n(D_p) dD_p, \quad (3)$$

188 where  $\rho_w$  is water density.

189 Similarly, the drizzle drop number concentration ( $N_d$ ) and liquid water content ( $LWC_d$ ) can be calculated  
 190 using the size distribution from 40  $\mu\text{m}$  to 1280  $\mu\text{m}$ . Particularly, the drizzle mean mass diameter ( $D_{mmd}$ )  
 191 is given by:

$$192 \quad D_{mmd} = \left( \frac{\int_{40}^{1280} D_p^3 n(D_p) dD_p}{\int_{40}^{1280} n(D_p) dD_p} \right)^{1/3}, \quad (4)$$

193 This quantity is chosen because the  $D_{mmd}$  denotes the diameter of average mass (the third-moment  
 194 average) of the drizzle size distribution, which provides the link between the number concentration and  
 195 the mass concentration of drizzle droplets in a sample (Hinds, 1999).

196 Adapting the method in Zheng et al. (2022b), the cloud base precipitation rate ( $R_{CB}$ ) is given by:

$$197 \quad R_{CB}(\text{mm/hr}) = 6\pi * 10^{-4} \int_{40\mu\text{m}}^{1280\mu\text{m}} D_{p,mm}^3 n(D_{p,mm}) U_{\infty}(D_{p,mm}) dD_{p,mm}, \quad (5)$$



198 in order to match the unit conversion, the  $D_{p,mm}$  is diameter in unit of mm,  $n(D_{p,mm})$  is drizzle number  
199 concentration in every size bin with a unit of  $\# \text{ m}^3 \text{ mm}^{-1}$ , and  $U_{\infty}(D_{p,mm})$  is terminal velocity in given  
200 size bin, which is calculated from the full Reynolds number theory as in Pruppacher and Klett (2010).

201 The combined threshold of  $N_c > 5 \text{ cm}^{-3}$  and  $LWC_c > 0.01 \text{ g m}^{-3}$  is used for determining the valid  
202 cloud samples and cloud boundaries (Wood, 2005; Zheng et al., 2022b). The complete cloud vertical  
203 profiles from sub-cloud to the above-cloud are selected during the ACE-ENA and SOCRATES IOPs, in  
204 which the flight strategy includes sawtooth and spiral cloud transects and ramping cloud sampling. The  
205 precipitation conditions are determined by whether samples of  $N_d > 0.001 \text{ cm}^{-3}$  exists below the cloud  
206 base height. In total, the selected numbers of cloud (precipitating cloud) profiles are 18 (13), 26 (13), and  
207 28 (24) for ACE-ENA summer and winter IOPs along with SOCRATES, respectively. The detailed  
208 selected cloud profiles, with their cloud base heights ( $z_t$ ), cloud top heights ( $z_b$ ) and cloud thicknesses  
209 ( $H_c = z_t - z_b$ ) are listed in Table S1, along with the cloud profile macrophysics.

210 Furthermore, the assessments of ACI are significantly impacted by the MBL dynamic and  
211 thermodynamic conditions. Jones et al. (2011) suggested that the MBL would be in a well-mixed and  
212 coupled condition when the difference in liquid water potential temperature ( $\theta_L$ ) and total water mixing  
213 ratio ( $q_t$ ) between the bottom of MBL and the inversion layer are less than 0.5 K and 0.5 g/kg,  
214 respectively. The cases selected for this study feature both coupled and decoupled MBL conditions,  
215 particularly during ACE-ENA summer, which is characterized by anomalously low MBL heights and  
216 substantial MBL decoupling. Previous studies found that, under the decoupled conditions, the aerosols,  
217 CCN, and moisture sources near the surface are disconnected from the cloud layer aloft, hence exerting  
218 much less effective impact on the cloud microphysics (Zheng et al., 2022a; Christensen et al., 2023; Su  
219 et al., 2024). Therefore, we adapt and modify the metric in Jones et al. (2011) to calculate the sub-cloud  
220 coupled layer, in order to quantify the degree to which aerosols and CCN measured sub-cloud are in a  
221 well-mixed state and can represent the actual interaction (or contact) with the cloud layer. In this study,

222 the  $q_t$  and  $\theta_L$  at the cloud base are calculated, and then their vertical variations are examined starting  
223 from the altitude of cloud base ( $z_b$ ) and looking downward. As such, the coupled point height ( $z_{cp}$ ) is  
224 defined as the altitude where the downward vertical changes in  $q_t$  and  $\theta_L$  exceed 0.5 K and 0.5 g/kg,  
225 respectively. Hence, the coupled layer thickness ( $H_{cp} = z_t - z_{cp}$ ) is defined as the layer between the  
226 cloud top height ( $z_t$ ) and coupled point height ( $z_{cp}$ ), hence the selection of the aerosols and CCN within  
227 the below-cloud part of the coupled layer can be viewed as in contact with the cloud. An example of the  
228 coupled layer identification is shown in Figure S2. Therefore, the degree of MBL decoupling ( $D_{cp}$ ) can  
229 be quantified as the ratio of the coupled point height ( $z_{cp}$ ) to the cloud base height ( $z_b$ ), where  $D_{cp} =$   
230  $z_{cp}/z_b$ . As shown in Table S1, the ACE-ENA summer feature with highest degree of decoupling  
231 (averaged  $D_{cp} = 0.504$ ), compared to the ACE-ENA winter ( $D_{cp} = 0.370$ ) and SOCRATES ( $D_{cp} = 0.277$ ).

232

## 233 **2.2 Aerosol properties**

234 The total aerosol number concentrations ( $N_a$ ) from ACE-ENA and SOCRATES are measured by  
235 the airborne Condensation Particle Counter (CPC) models 3772 and 3760A, which counts the number of  
236 aerosols with diameter ( $D_p$ ) larger than 3 nm and 11 nm, respectively (Kuang and Mei, 2019;  
237 SOCRATES Low Rate Data, 2022). Additionally, the Passive Cavity Aerosol Spectrometer (PCASP)  
238 onboard the ACE-ENA aircraft is capable of sizing the aerosol with  $D_p$  ranging from 0.1  $\mu\text{m}$  to 3.2  $\mu\text{m}$   
239 (Goldberger, 2020). While the ultra-high sensitivity aerosol spectrometer (UHSAS) measures the size-  
240 resolved aerosol distribution from 0.06  $\mu\text{m}$  to 1.0  $\mu\text{m}$  during SOCRATES (Uin, 2016). Therefore, the  
241 number concentrations of accumulation mode aerosols ( $N_{ACC}$ , 0.1  $\mu\text{m}$ -1  $\mu\text{m}$ ) can be discerned from the  
242 PCASP and UHSAS aerosol size distributions. The Aitken mode aerosols ( $N_{Ait}$ , < 0.1  $\mu\text{m}$ ) from the  
243 ACE-ENA is given by the fast integrated mobility spectrometer (FIMS), which can size the aerosol down  
244 to 9 nm (Olfert et al., 2008), while the  $N_{Ait}$  from SOCRATES is limited to 0.06  $\mu\text{m}$  – 0.1  $\mu\text{m}$  due to the  
245 limitation of UHSAS. As for the CCN measurements, the ACE-ENA utilized the Dual-Column CCN

246 Counter at two constant supersaturation levels of 0.15% and 0.35% (Uin and Mei, 2019), while the CCN  
247 number concentration ( $N_{CCN}$ ) during SOCRATES was measured under various supersaturation levels  
248 from 0.06% to 0.87% using a scanning CCN counter (Roberts and Nenes, 2005). In this study,  $N_{CCN}$  at  
249 0.35% supersaturation ( $N_{CCN0.35\%}$ ) is used to ensure a direct comparison between ACE-ENA and  
250 SOCRATES. The aerosol measurements are in the temporal resolution of 1Hz. Note that the aerosol and  
251 CCN data are quality-controlled by removing the data point where the  $N_c + N_d$  greater than  $5 \text{ cm}^{-3}$  or  $N_d$   
252 greater than  $0.01 \text{ cm}^{-3}$ , to filter out the contamination of the cloud droplets, and drizzle water splashing.

253 The sub-cloud aerosols and CCN are selected within the below cloud base part of the coupled  
254 layer, which is described in the last section, in order to better assess the aerosol-cloud interactions. The  
255 above-cloud aerosols and CCN are selected between the cloud top and 200 m above. Note that the  
256 selection criteria of 200 m above the cloud top would inevitably induce uncertainty in the cloud top ACI  
257 assessment, depending on the vertical trend of the individual aerosol profile. Over the Southeast Atlantic,  
258 Gupta et al. (2021) conducted an analysis focusing particularly on the differing impacts when biomass  
259 burning aerosols are in contact with marine stratocumulus cloud tops, using 100 m above as the  
260 demarcation, versus when they are separated by various distances, and found that significant differences  
261 were observed in cloud microphysics, owing to different droplet evaporation and nucleation, compared  
262 to separated profiles. That result is in agreement with the modeling sensitivity study over the Eastern  
263 North Atlantic by Wang et al. (2020), who found that aerosol plumes can exert impacts on the cloud-top  
264 microphysics only when they are in close contact with the cloud layer. In most cases, the ACE-ENA  
265 feature is a rather stable or slightly decreasing profile within a few hundred meters above the cloud top,  
266 while the long-range transports, particularly during summertime, will induce an elevated aerosol layer in  
267 higher altitudes that is not in contact with the cloud layer. The frequent new particle formation events  
268 during SOCRATES will significantly alter the free-troposphere Aitken mode aerosol budget, they would  
269 need to further subside to impact the cloud (McCoy et al., 2021; Zhang et al., 2023). Therefore, the 200

270 m criterion used in this study captures the close-to-cloud aerosol plumes and provides enough sample  
271 size for statistical analysis.

272

### 273 **3. Aerosol, cloud, and drizzle properties of selected cases**

#### 274 **3.1 Aerosols and CCN in above- and sub-cloud regimes**

275 The probability density functions (PDFs) of aerosols, CCN, and cloud microphysical properties  
276 from selected cases during the ACE-ENA and SOCRATES field campaigns are presented in Figure 1.  
277 Notably, the  $N_a$ ,  $N_{Acc}$  and  $N_{CCN0.35\%}$  values from the SOCRATES are the highest among the three IOPs,  
278 followed by the ACE-ENA summer and winter as illustrated in both above-cloud (Figs. 1a-1c) and sub-  
279 cloud regimes (Figs. 1d-1f). Such variations can be linked to the different aerosol sources in the ACE-  
280 ENA and SOCRATES regions, especially during the summer and winter seasons over the Azores.

281 In the SOCRATES region, according to the previous studies involving back-trajectory analyses,  
282 dominant air masses within the MBL primarily originate from the south or from the west, skirting the  
283 Antarctic coast (Zhang et al., 2023), while the air masses above the MBL follow a similar transport  
284 pathway, they can also originate from the tip of southern Africa and be transported southeast along the  
285 warm conveyor belt (McCoy et al., 2021). The SOCRATES above-cloud aerosols ( $674.6 \text{ cm}^{-3}$ ) are  
286 primarily constituted by the Aitken mode aerosols because the mean  $N_{Acc}$  is only  $62.5 \text{ cm}^{-3}$ . Previously,  
287 McCoy et al. (2021) reported average values of  $680.69 \text{ cm}^{-3}$ ,  $546.28 \text{ cm}^{-3}$  and  $465.05 \text{ cm}^{-3}$  for mid-  
288 troposphere, above and below cloud for the multiple SOCRATES cases, respectively. For individual  
289 cases, the above cloud aerosols vary from a couple hundred to over a thousand particles per cubic  
290 centimeter (McCoy et al., 2021; Zhang et al., 2023). These aerosols are predominantly produced from  
291 the oxidation of biogenic gases, notably the dimethyl sulfide (DMS) emitted by marine biological  
292 productivity (Sanchez et al., 2018; McCoy et al., 2020). The rising air currents in MBL transport these  
293 particles into the free troposphere (FT) with dominant aerosol population over the SO (McCoy et al.,  
294 2021; Sanchez et al., 2021). Hence, it reinforces the notion that the SO represents a pre-industrial marine

295 environment where the influence of anthropogenic and biomass-burning aerosols is mostly negligible  
296 (McCoy et al., 2020, 2021).

297         Conversely, the ENA region experiences aerosols of varied origins, spanning maritime air masses  
298 to those heavily influenced by continental emissions from North America or Northern Europe, especially  
299 during the summertime (Logan et al., 2014; Wang et al., 2020). The summertime air mass back-  
300 trajectories within the MBL strongly feature recirculating flow around the Azores high. During the  
301 wintertime, however, the air masses predominantly originate in the FT, are transported above the MBL,  
302 and are then further entrained down to the MBL by large-scale subsidence, indicating less influence from  
303 continental pollution (Y. Wang et al., 2021b). During the summer ACE-ENA campaign, the MBL is  
304 enriched by sulfate and carbonaceous particles (Y. Wang et al., 2021b; Zawadowicz et al., 2021). This  
305 enhancement is attributed both to local generation from DMS and to the long-range transport from the  
306 continental air masses, resulting in the mean  $N_a$  of  $312.6 \text{ cm}^{-3}$  and  $301.5 \text{ cm}^{-3}$  for above- and sub-cloud  
307 regimes, respectively. The ACE-ENA winter exhibits the lowest aerosol and CCN concentrations,  
308 predominantly sourced from local maritime influences, and coupled with reduced continental air mass  
309 intrusions (Zheng et al., 2018; Y. Wang et al., 2021b).

310         Figure 1a reveals that there are more above-cloud  $N_a$  during the three IOPs than sub-cloud values,  
311 especially during the SOCRATES. The higher above-cloud  $N_a$  values from the three IOPs are primarily  
312 contributed by Aitken mode aerosols because their corresponding  $N_{Acc}$  values are much lower (Figs.  
313 1a&b). It is interesting to note that the above-cloud  $N_{CCN0.35\%}$  values exceed the  $N_{Acc}$  for all three IOPs  
314 (Figs. 1b&c), implying that a significant fraction of Aitken mode aerosols can be activated to become  
315 CCN, corroborating findings from earlier studies (McCoy et al., 2021; Zheng et al., 2021). For the sub-  
316 cloud regime, the  $N_a$  values during SOCRATES and ACE-ENA winter are ~70-80% of their  
317 corresponding above-cloud values, and the  $N_a$  during ACE-ENA summer is almost identical to its above-  
318 cloud value. Notice that the sub-cloud  $N_{Acc}$  values from three IOPs are more than double the above-cloud

319  $N_{Acc}$  values, and most of the sub-cloud accumulation mode aerosol can be activated to become CCN at  
320 SS of 0.35%. It is interesting to note that the higher  $N_{CCN0.35\%}$  at sub-cloud layer during SOCRATES  
321 may partially result from the cloud process on aerosols (Figs. 1e&f), which is suggested by previous  
322 studies (McCoy et al., 2021; Zhang et al., 2023) and will be further discussed in Section 3.1.

323 To further investigate the above- and sub-cloud aerosol properties from three IOPs, the aerosol  
324 droplet size distributions are analyzed in Figure 2. It is evident that SOCRATES aerosols have the highest  
325 concentrations of Aitken mode particles ( $D_p = 0.06 - 0.1 \mu\text{m}$ , given that the  $< 0.06 \mu\text{m}$  is not available  
326 from UHSAS) for both the above- and sub-cloud regimes. McCoy et al. (2021) and Zheng et al. (2021)  
327 identified analogous origins and formations of the above-cloud Aitken mode aerosols over both the SO  
328 and ENA regions and concluded that these aerosols primarily originate from the nucleation of photo-  
329 oxidation products of DMS, notably  $\text{H}_2\text{SO}_4$  and MSA, in the free troposphere (FT). The differential  
330 concentrations can be ascribed to the fact that sea-surface DMS concentrations in the SO are generally  
331 higher than those in the ENA region (Aumont et al., 2002; Zhang et al., 2023). Moreover, DMS emissions  
332 in the ENA during summer surpass those during winter (Zawadowicz et al., 2021). For the accumulation  
333 mode aerosols ( $0.1 - 1 \mu\text{m}$ ), the  $N_{Acc}$  values for both above- and sub-cloud regimes during SOCRATES  
334 decrease monotonically with particle size. The results in Figure 2 further support the finding that Aitken  
335 mode aerosols are dominant over the SO. The  $N_{Acc}$  values during ACE-ENA show slight uplifts for the  
336 small accumulation mode aerosols ( $< 0.3 \mu\text{m}$ ), particularly for summer, reflecting the signal of potential  
337 long-range transport of fine-mode aerosols (Wang et al., 2020; Y. Wang et al., 2021b). Consequently,  
338 such comparison reinforces the notion that the SO represents a largely pre-industrial marine environment,  
339 wherein the influence of anthropogenic and biomass-burning aerosols is minimal (McCoy et al., 2020,  
340 2021; Zhang et al., 2023).

341 When contrasting the aerosol size distributions in the sub-cloud regime (Fig. 2b) with those in the  
342 above-cloud regime, the influence of cloud processing on aerosols is discernibly non-trivial, particularly

343 under the cloud-topped MBL conditions examined in this study. The FT aerosols can be entrained down  
344 and contribute to the population of Aitken mode aerosols within the MBL, and the sub-cloud aerosols  
345 can also be subject to the influence of new particle formation in the upper MBL, though arguably less  
346 effective than those within the FT (Zheng et al., 2021). Additionally, in-cloud Brownian capture can lead  
347 to a substantial reduction in Aitken mode aerosols (Hudson et al., 2015; Wyant et al., 2022), providing  
348 the rationale for the observed decrease in Aitken mode aerosols from above- to the sub-cloud regime,  
349 especially for particles smaller than 0.07  $\mu\text{m}$ . In addition, cloud chemical processing, such as the  
350 aqueous-phase condensation of sulfuric gas onto the aerosol cores inside the cloud droplets, is  
351 particularly pronounced during the transitioning of Aitken mode aerosols to accumulation mode aerosols  
352 (Hudson et al., 2015; Zhang et al., 2023).

353 From both above- to sub-cloud regimes, the larger Aitken mode aerosols ( $> 0.07 \mu\text{m}$ ) can be  
354 effectively enlarged to accumulation mode aerosols through coagulation and water vapor diffusional  
355 growth (Covert et al., 1996), contributing to the elevated accumulation mode aerosol distribution and  
356 increased  $N_{Acc}$  in the sub-cloud regime. These processes are evidenced by the decrease of critical  
357 supersaturations from above-cloud (between 0.35% - 0.4%) to sub-cloud (between 0.3% - 0.35%) during  
358 SOCRATES (Fig. S3) because the aerosol droplet sizes are enlarged and more readily become CCN.  
359 Furthermore, the collision-coalescence combines mixtures of large and small cloud droplets, and results  
360 in the sub-cloud aerosol residuals shifting towards the larger size upon the drizzle droplet evaporation  
361 below the cloud. This partially elucidates the observed increase in the tail-end of the accumulation mode  
362 aerosol distribution for all three IOPs. The elevation in sub-cloud coarse mode aerosols observed for both  
363 ACE-ENA IOPs (as seen in Fig. 2) can be attributed to the evaporation of collision-coalescence-enlarged  
364 drizzles and the intrusion of sea spray aerosols (e.g., sea salt), as illustrated and analyzed based on a  
365 summertime case study that exhibits the signal of cloud-processing aerosols (Zheng et al., 2022b), and  
366 the long-term aerosol physicochemical properties over the ARM-ENA ground-based observatory (Zheng  
367 et al., 2018) particularly during the winter season where the production of sea spray aerosol is prevalent.

368

### 369 **3.2 Bulk cloud microphysical properties distribution**

370 The PDFs of MBL cloud microphysical properties ( $N_c$ ,  $r_c$ ,  $LWC_c$ ) derived from aircraft in-situ  
371 measurements from the three IOPs are shown in Figures 1g-1i. The mean microphysical properties for  
372 the individual cloud profiles are listed in Table S2. The results in Figure 1 have demonstrated that  
373 aerosol/CCN sources and concentrations, especially from the sub-cloud regime, play an important role  
374 in cloud droplet formation and evolution. For example, the SOCRATES has the highest sub-cloud  
375 aerosols and CCN, and subsequently feature a larger number of smaller cloud droplets, given the highest  
376  $N_c$  ( $148.3 \text{ cm}^{-3}$ ) and smallest  $r_c$  ( $8 \text{ }\mu\text{m}$ ) among the three IOPs. These results have further confirmed and  
377 reassured our understanding of the aerosol first indirect effect: more aerosols induce more and smaller  
378 cloud droplets (higher  $N_c$  and smaller  $r_c$ ) under constrained liquid water content conditions, thus the  
379 MBL clouds reflect more incoming solar radiation (Twomey, 1977). The ACE-ENA wintertime clouds  
380 feature the fewest  $N_c$  ( $70.6 \text{ cm}^{-3}$ ) and largest  $r_c$  ( $9.8 \text{ }\mu\text{m}$ ), while the  $N_c$  and  $r_c$  ( $89.4 \text{ cm}^{-3}$  and  $9 \text{ }\mu\text{m}$ ) during  
381 ACE-ENA summer fall between the SOCRATES and ACE-ENA winter values. Considering the aerosol  
382 competing effect against the available water vapor, the relatively abundant aerosols in SOCRATES might  
383 account for the narrower  $r_c$  distribution, which peaks between  $6 - 10 \text{ }\mu\text{m}$ . SOCRATES has a lower cloud-  
384 layer water vapor mixing ratio (figure not shown) compared to ACE-ENA because the SO region has  
385 been observed to contain less precipitable water vapor than the ENA region due to the colder sea surface  
386 temperatures (Marcovecchio et al., 2023). Therefore, the aerosol and cloud properties in Figure 1 promise  
387 further examination of different cloud microphysical responses to aerosols via the ACI process. Note that  
388 the  $N_{CCN0.35\%}$  and  $N_c$  values are lower than  $N_c$  values during the ACE-ENA winter IOP, which is also  
389 confirmed in previous studies (J. Wang et al., 2022; Wang et al., 2023). This interesting phenomenon  
390 can potentially be attributed to a combination of factors, including lower MBL aerosol sources, stronger  
391 in-cloud coalescence-scavenging depletion of sub-cloud aerosols, and the aircraft snapshots capturing



392 the equilibrium states of aerosols and cloud due to enhanced aerosol activations induced by stronger  
393 updrafts during the ACE-ENA winter (J. Wang et al., 2022). This thereby compels further investigation  
394 into the potential impacts of precipitation on the MBL CCN budget. These aerosol-cloud-precipitation  
395 interactions (ACPIs) will be discussed in Section 4.

396

### 397 **3.3 Vertical distributions of cloud and drizzle microphysics**

398 The vertical distributions of the cloud and drizzle microphysical properties within the cloud layer  
399 from the three IOPs are shown in Figure 3. To ensure the representativeness of the vertical profiles, all  
400 the in-cloud samples are vertically smoothed using a triangular moving average method, and are inverse  
401 distance weighted in every 50 m moving altitude windows. Furthermore, the altitude is then normalized  
402 by  $z_i = \frac{Z - Z_{base}}{Z_{top} - Z_{base}}$ , where  $z_i = 0$  denotes cloud base and  $z_i = 1$  denotes cloud top. Consistent with  
403 previous discussions on the bulk microphysics distribution, the mean  $N_c$  values from SOCRATES are  
404 consistently higher than ACE-ENA summer and winter for the entire cloud layer, with a slight increase  
405 ranging from the cloud base to the upper-middle part ( $z_i \approx 0.85$ ) and then decreasing toward the cloud  
406 top due to cloud-top entrainment (Fig. 3a). All  $r_c$  values from the three IOPs show a near-linear increase  
407 from cloud base to top, with the smallest values observed during SOCRATES and the largest values  
408 observed during ACE-ENA winter (Fig. 3b).

409 The warmer and drier air near the cloud top entrains into the cloud layer and further mixes  
410 downward, often resulting in the evaporation of small cloud droplets and the shrinking of droplet sizes,  
411 which oppose condensational growth (Desai et al., 2021). Decreases in both  $N_c$  and  $LWC_c$ , and the  
412 reduced growth of  $r_c$  near the cloud top ( $z_i > 0.85$ ) support signals of cloud-top entrainment mixing  
413 during all three IOPs. It is interesting to note that the  $r_c$  values from SOCRATES increase monotonically  
414 from cloud base to top, while the  $r_c$  values from both ACE-ENA summer and winter increase until  $z_i \approx$   
415 0.8 and then remain nearly constant, although all of their  $N_c$  values (at  $z_i \approx 0.8$ ) decrease towards the

416 cloud top. When dry air entrainment occurs at the cloud top, some of the upper-level smaller cloud  
417 droplets will evaporate, which leads to decreases in  $N_c$  (Fig. 3a). As cloud-top entrainment mixing can  
418 shrink large cloud droplets via evaporation, depending on the entrainment mixing rate, the nearly  
419 constant  $r_c$  values (at  $z_i > 0.8$ ) might represent the equilibrium balance between two competing  
420 processes: cloud droplet condensational and collision-coalescence growths, and the entrainment mixing  
421 evaporation effects.

422 While carrying the distinct discrepancies in the mean values for all layers, the  $N_c$  and  $r_c$  from  
423 ACE-ENA summer and winter clouds experienced similar vertical evolutions as the SOCRATES. The  
424 increases of  $r_c$  ( $\Delta r_c$ ) from cloud base to cloud top are 4.03  $\mu\text{m}$ , 4.78  $\mu\text{m}$  and 5.85  $\mu\text{m}$ , with percentage  
425 increases of 66%, 68% and 79%, for SOCRATES, ACE-ENA summer and winter, respectively. Even  
426 though, theoretically, the condensational growth effect would be more pronounced on smaller cloud  
427 droplets due to their smaller surface area (Wallace and Hobbs, 2006), SOCRATES exhibits the thickest  
428 mean cloud thickness but experienced the least  $r_c$  increase among the three IOPs. This suggests that high  
429 aerosol loadings are limiting the overall growth of the cloud DSD in SOCRATES clouds, while the ACE-  
430 ENA winter clouds show the strongest  $r_c$  increase, in contrast. This comparison indicates different cloud  
431 microphysical responses to aerosol perturbations in the three IOPs, which will be further discussed in  
432 Section 4.1. The  $LWC_c$  values from the three IOPs are comparable to each other. The vertical  
433 distributions of MBL cloud microphysical properties examined in this study are in good agreement with  
434 the previous studies conducted on these two field campaigns (Wu et al., 2020a; Y. Wang et al., 2021a; J.  
435 Wang et al., 2021; Wang et al., 2023). In addition, the cloud adiabaticity is defined as  $f_{ad} =$   
436  $LWC_c/LWC_{ad}$ , where the  $LWC_{ad}$  denotes adiabatic LWC (Wu et al., 2020b). As shown in Figure S4,  
437 the clouds from all three IOPs feature certain levels of sub-adiabaticity above the cloud base. Considering  
438 the inter-cloud layer-mean  $f_{ad}$ , the campaign-mean  $f_{ad}$  values are  $0.689 \pm 0.229$ ,  $0.542 \pm 0.143$ , and  
439  $0.490 \pm 0.207$  for SOCRATES, ACE-ENA summer and winter, respectively. It is well known that cloud

440 sub-adiabaticity is primarily induced by the in-cloud collision-coalescence and the entrainment mixing  
441 processes (Hill et al., 2009; Braun et al., 2018; Gao et al., 2020; Wu et al., 2020b).

442 To quantitatively evaluate the impact of cloud-top entrainment mixing rate on cloud droplets, we  
443 adapt the method of Albrecht et al. (2016), where the cloud-top entrainment rate ( $w_e$ ) can be expressed  
444 as

$$445 \quad w_e = A_\sigma * \sigma_w / R_{i\sigma}, \quad (6)$$

446 where the turbulence kinetic energy (TKE) dissipation coefficient  $A_\sigma$  is empirically taken as 26 as in  
447 Albrecht et al. (2016), and the  $R_{i\sigma}$  is the buoyancy Richardson number calculated by  $(g/\theta_0) * (\Delta\theta_v h / \sigma_w^2)$ .  $\sigma_w$  denotes the standard deviation of vertical velocities taken near the cloud top ( $z_i > 0.9$ ),  
448 and  $h$  is the MBL height.  $\theta_0$  is the reference potential temperature and  $\Delta\theta_v$  is the virtual potential  
449 temperature difference across the temperature inversion layer above the cloud. Given the valid cloud top  
450 virtual potential temperature and vertical velocity measurements for the selected cloud cases, the  
451 averaged  $w_e$  values are  $0.570 \pm 0.834 \text{ cm s}^{-1}$ ,  $0.581 \pm 0.560 \text{ cm s}^{-1}$ , and  $0.960 \pm 1.127 \text{ cm s}^{-1}$  for SOCRATES,  
452 ACE-ENA summer and winter, respectively. The stronger  $w_e$  during ACE-ENA winter might be induced  
453 by the generally weaker cloud-top inversions and stronger near-cloud top turbulence, compared to the  
454 summertime when the ENA is dominated by the large-scale high-pressure system (Ghate et al., 2021).  
455 Considering the near cloud-top proportion of cloud where the  $LWC_c$  experienced decrease, the difference  
456 in  $LWC_c$  (between the cloud top value and the upper-middle cloud maximum for the mean profiles) for  
457 the ACE-ENA summer ( $-0.032 \text{ g m}^{-3}$ ) is higher than the reductions in winter ( $-0.018 \text{ g m}^{-3}$ ) and  
458 SOCRATES ( $-0.009 \text{ g m}^{-3}$ ), albeit that the  $w_e$  for ACE-ENA summer is comparable to SOCRATES, and  
459 much lower than ACE-ENA winter values. Within the above-cloud inversion layer, the temperature  
460 (water vapor mixing ratio) differences  $\Delta T$  ( $\Delta q$ ) are  $1.76 \text{ K}$  ( $-1.75 \text{ g kg}^{-1}$ ),  $1.54 \text{ K}$  ( $-1.66 \text{ g kg}^{-1}$ ) and  $1.48$   
461  $\text{K}$  ( $-1.09 \text{ g kg}^{-1}$ ) for SOCRATES, ACE-ENA summer and winter, respectively. Therefore, the warmer  
462 and dryer entrained air can partially contribute to the greater  $LWC_c$  reduction and the lower  $f_{ad}$  (0.39)

464 during the ACE-ENA summer than those during the ACE-ENA winter ( $f_{ad} = 0.45$ ) and SOCRATES  
465 ( $f_{ad} = 0.66$ ) near the cloud top (Fig. S4). For the three IOPs, the  $N_c$  and  $LWC_c$  exhibited stable trends  
466 from the cloud base, followed by noticeable decreases near the cloud top mixing zone, while the changes  
467 in  $r_c$  trends near the cloud top were not as dramatic as the others. Such characteristics of the cloud  
468 microphysics vertical profiles indicate the signal of inhomogeneous mixing, which occurs when dry and  
469 warm air mixes unevenly and slowly with the cloud air, hence partially evaporating the cloud droplets  
470 (Lehmann et al., 2009; Lu et al., 2011). The results are consistent with findings in stratocumulus clouds  
471 over multiple field campaigns (Brenquier et al., 2011; Jia et al., 2019) and with the findings for selected  
472 cases during the ACE-ENA (Yeom et al., 2021) and the SOCRATES (Sanchez et al., 2020). The near-  
473 cloud top  $r_c$  profiles ( $z_i > 0.8$ ) for the ACE-ENA cases exhibit fewer increases compared to the  
474 SOCRATES, which could be possibly attributed to more effective mixing due to the stronger entrainment  
475 rate, particularly during the ACE-ENA winter, eventually reaching a smaller equilibrium in terms of  
476 mean sizes.

477        Figures 3d-3f illustrate the normalized profiles of MBL drizzle microphysical properties. The  $N_d$   
478 values from the three IOPs mimic each other, which all maximize at the cloud top and then monotonically  
479 decrease toward the cloud base (Fig. 3d), while their  $LWC_d$  values follow a similar trend, albeit with  
480 relatively large differences (Fig. 3f). In contrast to the  $N_d$  and  $LWC_d$  trends, the  $D_{mmd}$  gradually increase  
481 from cloud top to cloud base (Fig. 3e), making physical sense since the drizzle droplets are typically  
482 formed near cloud top and continuously grow via collision-coalescence process while falling. The ACE-  
483 ENA wintertime drizzle  $D_{mmd}$  and  $LWC_d$  are distinctively larger than those in summertime and  
484 SOCRATES. It is interesting to note that near the cloud top ( $z_i > 0.9$ ), the ACE-ENA winter has  
485 comparable  $N_d$  but much larger  $D_{mmd}$  than the other two IOPs, suggesting that there were more large  
486 drizzle embryos formed from large cloud droplets (Fig. 3b) during ACE-ENA winter. It is noteworthy  
487 that the  $D_{mmd}$  in the lower-half region of the ACE-ENA winter clouds experienced rapid growth from

488 ~80  $\mu\text{m}$  to ~105  $\mu\text{m}$  (Fig. 3e), and this increment of ~25  $\mu\text{m}$  contributed to most of the  $D_{\text{mmd}}$  growth  
489 from cloud top to cloud base (33.5  $\mu\text{m}$ ), indicating a stronger warm-rain process during the winter.

490 In order to further analyze the cloud-to-drizzle conversion processes, the cloud and drizzle droplet  
491 size distributions (DSD) are categorized into four segments based on their relative position within the  
492 cloud layer (Fig. 4): upper cloud ( $z_i > 0.8$ , Fig. 4a), upper-middle cloud ( $0.5 \leq z_i < 0.8$ , Fig. 4b), lower-  
493 middle cloud ( $0.2 \leq z_i < 0.5$ , Fig. 4c) and lower cloud ( $z_i < 0.2$ , Fig. 4d). The cloud DSDs ( $D_p < 40$   
494  $\mu\text{m}$ ) from the three IOPs gradually shift towards larger sizes, moving from the lower to the upper cloud  
495 regions. This is accompanied by the narrowing of the cloud DSD ranges, as evidenced by the decline in  
496 the relative dispersion of cloud droplets ( $\epsilon$ ), which is defined as the ratio between the standard deviation  
497 and the mean radius of the distribution. At the lower portion of the cloud (Fig. 4d), the relatively greater  
498 value of  $\epsilon$  represents the co-existence of the newly formed small cloud droplets from recently activated  
499 CCNs and the sedimentation of larger droplets from the upper sections of the cloud. In addition, the  
500 discrepancies in  $\epsilon$  between the three IOPs may be attributed to the sub-cloud aerosol differences, which  
501 essentially resided in different microphysical regimes. Y. Wang et al. (2021a) stated that higher aerosol  
502 loading would lead to increased  $\epsilon$  due to the water vapor competition effect, supporting the discrepancy  
503 between SOCRATES and ACE-ENA summer IOPs, which can be categorized as a water-vapor-limited  
504 regime. Meanwhile, the ACE-ENA wintertime IOP exhibits characteristics of an aerosol-limited regime,  
505 in which the cloud DSDs tend to be narrower than in the water-limited regime, due to enhanced droplet  
506 growth, and the  $\epsilon$  values further decrease with height via the condensational narrowing effect (J. Chen et  
507 al., 2018).

508 Notably, the cloud DSDs during ACE-ENA winter exhibit a more pronounced negative skew (to  
509 the left) than those during ACE-ENA summer, which can be partially attributed to the activation of more  
510 sub-cloud coarse mode aerosols becoming larger cloud embryos, as demonstrated in Fig. 2. These coarse  
511 mode aerosols, whether from primary production of sea spray or the residuals of evaporated drizzle drops,

512 are more easily activated (or re-activated) into larger cloud droplets when they intrude (or recirculate)  
513 into the cloud layer (Hudson and Noble, 2020; Hoffmann and Feingold, 2023). Nevertheless, it is  
514 challenging to pinpoint the actual origins of coarse mode aerosols from the perspective of aircraft  
515 observational snapshots, thus requiring further numerical modeling work. For the four cloud portions  
516 from cloud base to cloud top, the skewness of summertime (wintertime) cloud DSDs are 0.627 (0.271),  
517 0.358 (0.175), 0.098 (-0.063), and -0.362 (-0.554), respectively. Ascending within the cloud, the process  
518 of water vapor condensation perpetually pushes the DSD towards larger sizes, culminating in a more  
519 negatively skewed DSD. Concurrently, the cloud-top entrainment mixing plays a pivotal role in  
520 minimizing  $\varepsilon$  in the upper cloud region, as elaborated by Lu et al. (2023). Note that in the upper region  
521 of the cloud (Fig. 4a), the ACE-ENA winter clouds contain more cloud droplets close to 40  $\mu\text{m}$ , albeit  
522 the mean  $N_c$  is lower. This scenario is conducive to the formation of larger drizzle embryos compared to  
523 summertime clouds, as depicted in Fig. 3e. In comparison, the SOCRATES clouds feature a pronounced  
524 log-normal DSD than the ACE-ENA, as the DSDs peak at  $D_p \sim 15 \mu\text{m}$  throughout the cloud, and  
525 subsequently, the lack of larger cloud droplets resulted in the smaller drizzle embryos near the cloud top.  
526 As the newly formed drizzle drops descend and continuously grow through the collision-coalescence  
527 process, the drizzle DSDs ( $D_p > 40 \mu\text{m}$ ) are noticeably broadened. From upper to lower cloud regions,  
528 the longer tails of the drizzle DSDs expand at the cost of smaller drizzle drops and cloud droplets via the  
529 collision-coalescence process. The clouds observed during ACE-ENA, especially in wintertime, contain  
530 more large drizzle drops ( $D_p > 200 \mu\text{m}$ ) than SOCRATES, which is reflected in the distinct differences  
531 in the vertical  $D_{mmd}$  as shown in Fig. 3e.

532 It has been intensively studied that in-cloud turbulence can stimulate collision-coalescence and  
533 consequently enhance the drizzle evolution processes (Pinsky et al., 2007; Grabowski and Wang, 2013;  
534 Wu et al., 2017; S. Chen et al., 2018). The turbulence strength is characterized by the turbulence kinetic  
535 energy (TKE), which is calculated as:

536  $TKE = \frac{1}{2}(\overline{u'^2} + \overline{v'^2} + \overline{w'^2})$ , (7)

537 where the turbulent perturbations of vertical ( $\overline{w'^2}$ ) and horizontal ( $\overline{u'^2}$  and  $\overline{v'^2}$ ) components are  
538 calculated as the simple moving variance in a 10s window centered at the measurement time, without  
539 window weighting function, using 1Hz data for all three IOPs. The  $w$  data is confined to an absolute  
540 aircraft roll angle of less than  $5^\circ$  (Cooper et al., 2016). Given the average aircraft ground speed of  $\sim 140$   
541 m/s and vertical speed of  $\sim 5$  m/s (Atlas et al., 2020), the smallest resolved wavelength is 140 m. Hence,  
542 within the 10s moving window, the  $\sim 50$  m in the integral vertical range is able to resolve the eddies up  
543 to  $\sim 1400$  m in size, and preserve the potential of capturing the inertial subrange.

544 As shown in Figure 5, the vertical wind variances (Fig. 5b) in ACE-ENA winter (layer-mean of  
545  $0.244 \text{ m}^2 \text{ s}^{-2}$ ) are generally higher than those in summer ( $0.153 \text{ m}^2 \text{ s}^{-2}$ ) and SOCRATES ( $0.147 \text{ m}^2 \text{ s}^{-2}$ ),  
546 while the horizontal wind variances (Fig. 5c & d) are comparable between ACE-ENA winter and summer  
547 but much higher than the SOCRATES, resulting in higher TKE during ACE-ENA. Note that the higher  
548  $w'^2$  near cloud top corresponds to the stronger entrainment rate in wintertime ACE-ENA. Near the cloud  
549 top, turbulence effectively enhances coalescence between the larger cloud droplets, primarily by  
550 increasing the relative velocities between droplets (Magaritz-Ronen et al., 2016; Ghate and Cadeddu,  
551 2019), and this is especially true for the vertical component  $w'^2$  of TKE. While the horizontal turbulence  
552 components, the  $u'^2$  and  $v'^2$  can also play a role in mixing the ambient air masses and contribute to the  
553 broadening of DSD (Wu et al., 2017). The use of TKE provides an illustration that in-cloud turbulence  
554 during ACE-ENA might be slightly stronger than that observed during SOCRATES. That being said, the  
555 quantitative evaluation of the turbulent enhancement of collision-coalescence requires access to the eddy  
556 dissipation rate, as typically used in model parameterizations (Grabowski and Wang, 2013; Witte et al.,  
557 2019). The smallest scales resolvable with the 1Hz measurement used in this study are on the order of  
558 140 meters, thus capturing only the larger-scale end of the inertial subrange and larger turbulent motions.  
559 Consequently, the ability to resolve smaller eddies and turbulent structures, crucial for understanding the

560 energy cascade within the inertial subrange, is limited by the too-coarse spatial and temporal resolutions  
561 and aliasing issues (Siebert et al., 2010; Muñoz-Esparza et al., 2018; Kim et al., 2022). Therefore, to  
562 fully resolve the spectrum of turbulence and quantitatively examine energy dissipation and mixing  
563 processes, access to higher-frequency measurements is required to capture smaller eddies within the  
564 inertial subrange (Siebert et al., 2010; Lu et al., 2011; Waclawczyk et al., 2017). Additionally, further  
565 quantifying the entrainment-mixing mechanisms also requires high-frequency eddy dissipation and  
566 accurate examination of the mixing time scale (Lehmann et al., 2009; Lu et al., 2011) for individual  
567 profiles. Though currently beyond the scope of this study, utilizing the high-rate measurements of  
568 velocities available from SOCRATES (at 25Hz) and ACE-ENA (at 20Hz) to explore those mechanisms  
569 further will be of interest to future investigations.

570 Drizzle formation and evolution in the ACE-ENA winter clouds are noticeably stronger than in  
571 the other two IOPs, which could be attributed to multiple factors. First, the ambient aerosols and CCN  
572 during winter are substantially fewer, featuring clean environments that promote the formation of  
573 generally larger cloud droplets due to the availability of more water content per droplet. Larger cloud  
574 droplets are more likely to collide and coalesce into drizzle drops, leading to relatively heavier  
575 precipitation (Chen et al., 2011; Duong et al., 2011; Mann et al., 2014). Furthermore, the wintertime  
576 clouds feature deeper cloud layers with mean thickness of (392.4 m) compared to the summertime clouds  
577 (336.3). In a thicker cloud layer with sufficient turbulence, the residence times of large cloud droplets  
578 and drizzle drops are elongated, and the chance of collision-coalescence growth can be effectively  
579 increased by recirculating the drizzle drops (Brost et al., 1982; Feingold et al., 1996; Magaritz et al.,  
580 2009; Ghate et al., 2021). Additionally, the prevalence of precipitation-evaporation-induced MBL cold  
581 pools, which disturb the MBL thermodynamics and contribute to turbulent mixing (Zuidema et al., 2017),  
582 during the wintertime might provide strong dynamical forcing to the warm-rain process (Jenson et al.,  
583 2021; J. Wang et al., 2022; Smalley et al., 2024). As a result, the ACE-ENA wintertime drizzle DSD is  
584 sufficiently broadened, and the  $D_{mmd}$  is enlarged toward the cloud base. In comparison, although the



585 SOCRATES exhibits even thicker clouds (487.4 m), the drizzle processes are seemingly suppressed by  
586 the much higher ambient aerosol and CCN concentrations.

587

## 588 **4 Aerosol-cloud-precipitation interactions (ACPIs)**

### 589 **4.1 Cloud microphysical responses on aerosols**

590 The impacts of different aerosol loadings on the cloud microphysical properties can be assessed  
591 by the aerosol-cloud interaction (ACI) indices, which can be quantified as:

$$592 \quad ACI_N = \frac{\partial \ln(N_c)}{\partial \ln(N_{CCN,0.35\%})}, \quad (8)$$

593 and

$$594 \quad ACI_r = -\frac{\partial \ln(r_c)}{\partial \ln(N_{CCN,0.35\%})}, \quad (9)$$

595 which emphasizes the cloud microphysical responses to CCN via the relative logarithmic change of  $N_c$   
596 and  $r_c$  to the change in  $N_{CCN,0.35\%}$  (Feingold et al., 2003; McComiskey et al., 2009). Physically, the ACI  
597 process involves aerosols intruding into the cloud layer, activating as cloud droplets, and subsequently  
598 altering cloud DSD and dispersion (Zheng et al., 2022a&b) under various water vapor availabilities.  
599 Therefore, the cloud microphysical responses within the lower region of the cloud are assessed, which is  
600 the first stage in which the sub-cloud CCN can directly interact with the cloud droplets. Furthermore, the  
601 similarity in the vertical integral of  $LWC_c$  (as shown in Fig. 3c) provides comparable liquid water  
602 between three IOPs for the assessment of newly generated cloud embryos from activated CCN because  
603 the  $ACI_r$  is normally assessed under a fixed liquid water (Zheng et al., 2020).

604 Considering all the cases from three IOPs with available CCN measurements (some cases without  
605 CCN measurements during SOCRATES), the  $N_c$  and  $r_c$  at the lower cloud ( $z_i < 0.2$ ) are plotted against  
606 the sub-cloud  $N_{CCN,0.35\%}$  in Figure 6, and the ACI indices are calculated as  $ACI_{N,CB}$  and  $ACI_{r,CB}$  (CB  
607 denoting the assessment near the cloud base). Note that the availability of valid sub-cloud measurements  
608 inevitably limits the sample size, especially for SOCRATES, as shown in Table S2. As shown in Figure

609 6a, the  $ACI_{N,CB}$  for the ACE-ENA wintertime (0.748) is higher than the summertime (0.617), indicating  
610 that  $N_c$  is more sensitive to the sub-cloud  $N_{CCN,0.35\%}$  during the winter. In other words, aerosols intruding  
611 into the cloud layer are easily activated to become cloud droplets. The  $N_c$  sensitivity for the SOCRATES  
612 cloud (0.692) lies between the two ACE-ENA IOPs. The  $ACI_{N,CB}$  values from three IOPs are generally  
613 higher than the  $ACI_N$  values from the layer-mean  $N_c$  against the sub-cloud  $N_{CCN,0.35\%}$  (not shown).  
614 Previous studies have shown that the enhanced vertical turbulence (updraft velocity) can effectively  
615 facilitate CCN replenishment into the cloud layer (Hu et al., 2021; Zheng et al., 2022a&b) and increase  
616 the actual in-cloud supersaturation (Brunke et al., 2022), thus leading to a more efficient cloud droplet  
617 formation, enhancing the  $ACI_{N,CB}$ . By correlating the mean TKE values with the CCN activation ratio  
618 ( $N_c/N_{CCN,0.35\%}$ ) for all individual cloud cases, the three IOPs show moderate but statistically significant  
619 correlation coefficients of 0.36, 0.55, and 0.51 for ACE-ENA summer, winter, and SOCRATES,  
620 respectively. This result reinforces the notion that the CCN activation fractions, particularly during the  
621 wintertime ACE-ENA, are significantly correlated with in-cloud turbulence intensities. Furthermore,  
622 more coarse mode aerosols during ACE-ENA winter are also favorable to the activation efficiency  
623 (Dusek et al., 2006).

624 As for the  $r_c$  responses to CCN (Fig. 6b), the typical Twomey effect, where more CCN compete  
625 against available water vapor and result in smaller cloud droplets, is evidenced by different cloud  
626 susceptibility between the three IOPs. The SOCRATES features a higher  $ACI_{r,CB}$  (0.311), suggesting  
627 that an increase in  $N_{CCN,0.35\%}$  can result in a significant decrease in  $r_c$ , compared to ACE-ENA summer  
628 (0.206) and winter (0.263). Although the absolute range of variation for  $r_c$  during SOCRATES is smaller,  
629 the slope is much deeper (Fig. 6b). Recall that the sub-cloud  $N_{CCN,0.35\%}$  during SOCRATES is generally  
630 higher and is constituted by more small-sized aerosols (as indicated in Fig. 2b). Consequently, after  
631 activation, the lower part of the cloud exhibits a higher number of smaller cloud droplets, as shown in  
632 Fig. 4d, even under the relatively less  $N_{CCN,0.35\%}$  condition for SOCRATES. Therefore, as more CCN

633 intrudes into the cloud, the competition for water vapor among newly-activated cloud droplets becomes  
 634 more pronounced, given similar water availability. In contrast, the presence of larger cloud droplets near  
 635 the cloud base, whether activated from coarse-mode aerosols or remaining as residuals from collision-  
 636 coalescence, would elevate the  $r_c$  especially under the relatively more CCN condition, hence inevitably  
 637 dampening the  $ACI_{r,CB}$  during ACE-ENA. However, a more comprehensive investigation into the cloud  
 638 microphysical responses to CCN intrusions under a larger range of various water supply conditions, and  
 639 further untangling the ACI from the meteorological influences, will require additional aircraft cases from  
 640 more field campaigns, for instance the VAMOS Ocean-Cloud-Atmosphere-Land Study (VOCALS), the  
 641 Cloud System Evolution over the Trades (CSET), the ObseRvations of CLOUDs above Aerosols and their  
 642 intERactionS (ORACLES), and the Aerosol Cloud meTeorology Interactions oVer the western ATlantic  
 643 Experiment (ACTIVATE). Note that the  $ACI_{r,CB}$  values in Figure 6b are also larger than the results from  
 644 the layer-mean  $r_c$  against sub-cloud  $N_{CCN,0.35\%}$ , since the layer-mean microphysics is more subject to the  
 645 cloud droplet evolution processes such as condensational growth and collision-coalescence. The ACI  
 646 indices from three IOPs are in the ACI range of the previous studies in MBL clouds (Twohy et al., 2005;  
 647 Lu et al., 2009; Diamond et al., 2018) using aircraft in-situ measurements.

648 To investigate the ACI indices at the upper level of the cloud, the  $N_c$  and  $r_c$  at the upper cloud  
 649 ( $z_i > 0.8$ ) are plotted against the above-cloud  $N_{CCN,0.35\%}$  in Figure S5, and the ACI indices are calculated  
 650 as  $ACI_{N,CT}$  and  $ACI_{r,CT}$  (denoting the assessments near the cloud top). Compared to the  $ACI_{N,CB}$  and  
 651  $ACI_{r,CB}$ , the  $ACI_{N,CT}$  and  $ACI_{r,CT}$  are much weaker, especially for  $ACI_{r,CT}$ , as the near cloud top droplets  
 652 are too large for above-cloud aerosols to exert a significant influence on  $r_c$  (Diamond et al., 2018; Gupta  
 653 et al., 2022). While the weaker cloud top  $N_c$  dependence on the  $N_{CCN,0.35\%}$  could be due to the legacy of  
 654 the sub-cloud CCN impacts on  $N_c$  being conveyed to the cloud top. This occurs because FT aerosols and  
 655 CCN can be entrained down to the MBL before and during the cloud process, as observed in the  
 656 assessment of inter-cloud cases. These weaker relationships support the notion that although the aerosols

657 entrained into the upper-cloud region can affect the cloud microphysics to a certain degree, the effects  
658 are less pronounced than those from the sub-cloud aerosols (Diamond et al., 2018, Wang et al., 2020)  
659 because the MBL cloud  $N_c$  and  $r_c$  variations are dominated by the condensational growth, collision-  
660 coalescence, and entrainment mixing processes near the cloud top.

661

## 662 **4.2 Precipitation susceptibility**

663 The precipitation susceptibility relies on the assessment of relative responses in the precipitation  
664 rate to the change in  $N_c$  (Feingold and Seibert, 2009; Sorooshian et al., 2009), which is defined as:

$$665 S_o = -\frac{\partial \ln(R_{CB})}{\partial \ln(N_c)}, \quad (10)$$

666 where the  $R_{CB}$  is the cloud base precipitation rate calculated in section 2 (equation 5). By incorporating  
667 all the cloud cases, including both precipitating and non-precipitating clouds (the  $R_{CB}$  can also be  
668 calculated based on the drizzle DSD near the cloud base), the  $S_o$  accounts for the impact of cloud droplets  
669 on the potential precipitation ability of the cloud (Terai et al., 2012).

670 As shown in Figure 7a, the  $R_{CB}$  values generally have a negative correlation with increased layer-  
671 mean  $N_c$  for all three IOPs. The  $S_o$  values are 0.979, 1.229, and 1.638, with the absolute values of  
672 correlation coefficients being 0.33, 0.29, and 0.45 for SOCRATES, ACE-ENA summer and winter,  
673 respectively. These correlation coefficient values fall within the reasonable range found in previous  
674 studies on precipitation susceptibility in MBL stratus and stratocumulus clouds (Jung et al., 2016; Gupta  
675 et al., 2022), and indicate statistically significant dependences of  $R_{CB}$  on  $N_c$ . Previous study by Terai et  
676 al. (2012) found that the  $S_o$  values decrease with the increasing cloud thickness over the southeast Pacific,  
677 and Jung et al. (2016) found that the  $S_o$  is more pronounced within the medium-deep clouds with  
678 thickness ~300-400 m in the MBL stratocumulus over the eastern Pacific. While Gupta et al. (2022)  
679 found that the  $S_o$  values are generally higher under low ambient  $N_a$  condition in the southeastern Atlantic  
680 MBL. In this study,  $R_{CB}$  for the ACE-ENA winter is more susceptible to the layer-mean  $N_c$  than the

681 ACE-ENA summer and SOCRATES, which can be partially attributed to the existence of more large  
682 drizzle drops (as shown in Fig. 4d) near the cloud base. As previously discussed, the ACE-ENA winter  
683 featured enhanced collision-coalescence and drizzle-recirculating processes, especially under low  $N_c$   
684 conditions with more large drizzle drops, leading to the increase of  $S_o$  values. In comparison, the higher  
685 ambient aerosol and CCN concentrations during SOCRATES lead to relatively narrower drizzle DSDs  
686 and may induce effective aerosol buffering effects, where the warm-rain processes in cloud are already  
687 fairly suppressed, hence diminishing the sensitivity of  $R_{CB}$  to  $N_c$  (Stevens and Feingold, 2009; Fan et al.,  
688 2020; Gupta et al., 2022).

689 It is well known that the  $R_{CB}$  can be parameterized or predicted via an approximate relation with  
690  $N_c$  and cloud thickness ( $H_c$ ), which is usually parameterized in the form of  $R_{CB} \propto c H_c^3 N_c^{-1}$  (Lu et al.,  
691 2009; Kang et al., 2024). Following the same method, we derive the relationships from three IOPs in  
692 Figure 7b, where the  $R_{CB}$  are positively (negatively) proportional to the  $H_c$  ( $N_c$ ), with the exponential  
693 parameters in the range of the typical values in the MBL clouds (Comstock et al., 2004; vanZanten et al.,  
694 2005; Lu et al., 2009). The statistical coefficient of determination ( $R^2$ ) values of  $R_{CB}$  against  $H_c$  ( $N_c$ ) are  
695 0.696 (0.177), 0.419 (0.212) and 0.165 (0.295), for the ACE-ENA summer, winter and SOCRATES,  
696 respectively, suggesting that the  $R_{CB}$  in ACE-ENA clouds may be more determined by  $H_c$ , while the  
697  $R_{CB}$  in SOCRATES cloud are more related to  $N_c$ . Note that the relationship for SOCRATES in this study  
698 reveals a similar  $R_{CB}$  dependence on  $N_c$  but a smaller dependence on the cloud thickness than the study  
699 by Kang et al. (2024), who concluded a relationship of  $R_{CB} = 1.41 \times 10^{-9} H_c^{3.1} N_c^{-0.8}$ , based on the rain  
700 rate retrieved from radar and lidar measurements and the aerosol concentration also from the  
701 SOCRATES. The discrepancies are possibly due to the different sample selections and different methods  
702 in the  $R_{CB}$  calculation. Note that the mean cloud thicknesses of the ACE-ENA summer (336.3 m), winter  
703 (392.4 m) and SOCRATES (487.4 m), are within the thickness range found to exhibit stronger  $S_o$  (Terai  
704 et al., 2012; Jung et al., 2016; Gupta et al., 2022).

705

### 706 **4.3 Drizzle impacts on sub-cloud CCN and implication to ACI**

707 Multiple studies on the MBL clouds have concluded that the in-cloud drizzle formation and  
708 evolution processes can effectively impact the sub-cloud CCN budgets via the coalescence-scavenging  
709 effect (Wood, 2006; Wood et al., 2012; Diamond et al., 2018; Zheng et al., 2022b; Zhang et al., 2023).  
710 Drizzle drops are formed and grow via the collision-coalescence process by collecting cloud droplets and  
711 small drizzle drops, resulting in the consumption of CCN (the precursor of cloud droplet), but in the  
712 meantime, the in-cloud  $N_c$  can be continuously buffered by the sub-cloud CCN replenishment. Although  
713 the sub-cloud aerosols (especially in large size) would be added if the drizzle fell and evaporated outside  
714 the cloud, the increment cannot compensate for the loss. Therefore, the net result of the whole process is  
715 usually presented as the depletion of sub-cloud CCN residuals, and such drizzle modulation on the CCN  
716 budget could be substantial in moderate-to-light drizzles or even non-precipitating clouds, depending on  
717 the collision-coalescence efficiency (Feingold et al., 1996; Wood, 2006; Kang et al., 2022).

718 The CCN loss rate due to the coalescence-scavenging effect can be calculated as:

$$719 L_{CCN} = -\frac{K H_c}{H_{cp}} * N_c * R_{CB}, \quad (11)$$

720 where the constant  $K$  ( $2.25 \text{ m}^2 \text{ kg}^{-1}$ ) denotes the drizzle collection efficiency (Wood et al., 2006; Diamond  
721 et al., 2018).  $H_c$  is cloud thickness, and  $H_{cp}$  is the coupled layer thickness to ensure the change in the  
722 cloud layer can be sufficiently conveyed throughout the layer. The calculated CCN loss rate for individual  
723 cases is listed in Table S2. Considering all cloud (precipitating cloud) scenarios, the mean CCN loss rates  
724 are  $-7.69 \pm 13.96 \text{ cm}^{-3}\text{h}^{-1}$  ( $-10.45 \pm 15.56 \text{ cm}^{-3}\text{h}^{-1}$ ),  $-6.29 \pm 11.65 \text{ cm}^{-3}\text{h}^{-1}$  ( $-12.11 \pm 14.64 \text{ cm}^{-3}\text{h}^{-1}$ ), and -  
725  $4.94 \pm 7.96 \text{ cm}^{-3}\text{h}^{-1}$  ( $-5.58 \pm 8.43 \text{ cm}^{-3}\text{h}^{-1}$ ) for ACE-ENA summer, winter and SOCRATES, respectively.  
726 As the results indicate, the ACE-ENA clouds experience more substantial sub-cloud CCN loss than  
727 SOCRATES, especially in wintertime precipitating clouds. Recall that the assessment of  $ACI_{r,CB}$  relies  
728 on the relative changes of  $r_c$  and  $N_{CCN}$ , while the different  $L_{CCN}$  for individual cases can result in the

729 shrinking of the  $N_{CCN}$  variation ranges (imagine the abundant CCN are depleted by the coalescence-  
730 scavenging). In other words, the given change in  $r_c$  corresponds to a narrowed change in  $N_{CCN}$ .  
731 Mathematically speaking, the assessment of  $ACI_{r, CB}$  depends on the ratio of the numerator (change in  $r_c$ )  
732 and the denominator (change in  $N_{CCN}$ ). Under the circumstances of substantial cloud-processing to the  
733 aerosols, the altered sub-cloud CCN budgets are reflected as a smaller denominator, versus the less  
734 altered numerator, hence mathematically presented as an enlarged  $ACI_{r, CB}$ . Therefore, the coalescence-  
735 scavenging effect can not only deplete the sub-cloud CCN, but also quantitatively amplify the assessment  
736 of cloud microphysics susceptibilities (Feingold et al., 1999; Duong et al., 2011; Jung et al., 2016; Zheng  
737 et al., 2022b). In order to examine the potential impact of the aforementioned processes on the  $ACI$   
738 assessment, a sensitivity analysis is conducted by simply retrospectively the sub-cloud  $N_{CCN0.35\%}$   
739 according to their  $L_{CCN}$ . For each retrospective time step  $\Delta T$ , the  $r_c$  values are held unchanged, and the  
740 retrospective  $N_{CCN0.35\%}$  values for individual cloud cases are given by  $N_{CCN0.35\%} - L_{CCN} * \Delta T$ , and then  
741 the  $ACI_{r, CB}$  can be recalculated. Note that assuming a constant  $r_c$  value over time inevitably induces  
742 uncertainty and biases, as it does not consider the microphysical processes affecting the cloud droplet  
743 mean size. However, previous numerical experiments show that the noticeable impact on the cloud mean  
744 radius through collision-coalescence necessitates a high degree of CCN depletion, and the quantified  
745 percentage changes in droplet mean sizes are several times less than the changes in CCN depletion  
746 (Feingold et al., 1996). Hence, the retrospective method, from an observational snapshot point of view,  
747 provides a direction that enables the assessment of  $ACI_{r, CB}$  as if before the sub-cloud aerosols and CCN  
748 are scavenged by in-cloud coalescence-scavenging and precipitation scavenging processes.

749 As shown in Figure 8, the  $ACI_{r, CB}$  values tend to decrease with the retrospective time, which  
750 indicates the retrospective CCN variation range is enlarged and counteracting the coalescence-  
751 scavenging amplification. The detailed illustration of the different  $ACI_{r, CB}$  calculated from the scattered  
752  $r_c$  and sub-cloud  $N_{CCN0.35\%}$  is shown in Figure S6. Note that the  $ACI_{r, CB}$  decreasing rates for the

753 precipitating clouds (Fig. 8b) are not as strong as for all clouds because the non-precipitating clouds have  
754 smaller  $L_{CCN}$  largely due to weaker collision-coalescence. Hence, the retrospective time scale might  
755 quickly exceed the actual time of the cloud-processing effects on the aerosol and CCN. In other words,  
756 the time needed, to restore the sub-cloud CCN to the budget before the cloud-processing, is shorter. Thus,  
757 results in the faster decrease of  $ACI_{r,CB}$  in the non-precipitating cloud. The retrospective of the sub-cloud  
758 CCN budget will yield an alternative assessment of ACI, assuming that the drizzle processes have not  
759 yet significantly impacted the sub-cloud CCN budget, especially for the assessment under the  
760 precipitating clouds. However, examining the exact precipitating timing is challenging since the aircraft  
761 provides a snapshot of the cloud and aerosol information. Thus, this retrospective study only provides a  
762 possible direction, and the result should be interpreted with caution.

763

## 764 **5. Summary and Conclusions**

765 Based on the aircraft in-situ measurements during ACE-ENA and SOCRATES, the vertical  
766 distributions and the evolutions of the aerosol, cloud, and drizzle properties are investigated under the  
767 cloud-topped MBL environments. The aerosols and CCN from SOCRATES are the highest among the  
768 three IOPs, followed by ACE-ENA summer and winter in descending order in both above- and sub-cloud  
769 regimes. The differences can be attributed to the differences in aerosol size distributions between ACE-  
770 ENA and SOCRATES, which are largely due to the aerosol sources in those regions. The SOCRATES  
771 features the pre-industrial natural environment enriched by aerosols from marine biological productivity  
772 and without the contamination of anthropogenic aerosols, while the ACE-ENA features the aerosols from  
773 varied sources, including maritime and continental emissions, with distinct seasonal variations.  
774 Examining the aerosol size distributions in sub-cloud versus above-cloud regimes manifests the  
775 significant influence of cloud processing on aerosols. Physical processing like in-cloud Brownian capture  
776 can reduce Aitken mode aerosols, while the chemical processes transform Aitken mode aerosols to larger  
777 sizes, moving them toward the accumulation mode. In addition, the in-cloud coalescence processes shift



778 sub-cloud aerosol residuals to larger sizes, as multiple aerosols combine into a single aerosol core inside  
779 the cloud droplet during collision-coalescence, explaining the observed increase in the tail-end of the  
780 aerosol distribution for all IOPs.

781 As for the cloud and drizzle properties, the SOCRATES clouds feature more and smaller cloud  
782 droplets than the ACE-ENA summertime and wintertime clouds, with the  $r_c$  growths (and percentage  
783 increases), from cloud base to top, being  $4.03 \mu\text{m}$  (0.66%),  $4.78 \mu\text{m}$  (0.68%), and  $5.85 \mu\text{m}$  (0.79%) for  
784 SOCRATES, ACE-ENA summer, and winter, respectively. The cloud-top entrainment mixing is  
785 evidenced in the observed decline of both  $N_c$  and  $LWC_c$  near the cloud top. The mean cloud-top  
786 entrainment rates ( $w_e$ ) are  $0.570 \pm 0.834 \text{ cm s}^{-1}$ ,  $0.581 \pm 0.560 \text{ cm s}^{-1}$ , and  $0.960 \pm 1.127 \text{ cm s}^{-1}$  for  
787 SOCRATES, ACE-ENA summer and winter, respectively. The strongest  $w_e$  during ACE-ENA winter is  
788 owing to weaker cloud-top inversions and stronger near-cloud-top turbulence. The values of the TKE for  
789 three IOPs are generally within the ranges of previous studies (Atlas et al., 2020; Ghate et al., 2021). For  
790 drizzle vertical distribution,  $N_d$  from the three IOPs all exhibit decreases from cloud top to cloud base,  
791 while  $D_{mmd}$  are in opposite directions with a maximum at the cloud base. The ACE-ENA wintertime  
792 clouds feature more prominent drizzle formation and evolution owing to the combined effects of  
793 relatively cleaner environment, deeper cloud layer, and slightly stronger in-cloud vertical turbulence,  
794 which substantially enhances the collision-coalescence and the drizzle re-circulating processes,  
795 compared to the other two IOPs. While satellite retrievals of droplet number concentration heavily rely  
796 on the adiabatic cloud assumption and are usually given as a constant of  $f_{ad} = 0.8$ , the in-situ  
797 observational evidence found in this study further confirms the unrealistic nature of this assumption. It  
798 will be of interest to utilize multiple aircraft measurements (campaigns) to explore the variability of MBL  
799 cloud and drizzle microphysical properties over different marine regions. This can help examine potential  
800 predictors for  $f_{ad}$ , which will aid in satellite-based retrievals and aerosol-cloud interaction assessments  
801 (Painemal and Zuidema, 2011; Grosvenor et al., 2018; Painemal et al., 2021).

802 Comparing the seasonality of cloud base precipitation rate ( $R_{CB}$ ) during ACE-ENA, more cases  
803 with large observed  $R_{CB}$  during the winter season, which is consistent with J. Wang et al. (2022). Notably,  
804 the sensitivity of  $R_{CB}$  to  $N_c$  is more pronounced for the ACE-ENA during both winter (with precipitation  
805 susceptibility  $S_o = 1.638$ ) and summer ( $S_o = 1.229$ ) compared to the SOCRATES ( $S_o = 0.979$ ). This is  
806 partly due to the much higher  $R_{CB}$  induced by larger drizzle drops near the cloud base for ACE-ENA, a  
807 result of turbulence-driven in-cloud droplet interactions, especially under low  $N_c$  condition. Furthermore,  
808  $R_{CB}$  can be approximated by a relationship involving  $N_c$  and  $H_c$ , as suggested in prior research. The  
809 relationships established in this study indicate that ACE-ENA clouds, are largely determined by  $H_c$ ,  
810 while SOCRATES clouds are more influenced by the  $N_c$ . The combination of a deeper cloud layer and  
811 relatively lower ambient aerosol concentration, eventually leading to stronger drizzle production and  
812 evolution during ACE-ENA, especially during the winter season, results in more robust precipitation  
813 susceptibility. Note that considering the combined factors of aerosol loadings, cloud morphology and  
814 thicknesses, and the assessment methodology, the derived  $S_o$  values in this study are generally higher (or  
815 close to the upper end) compared to previous studies (Lu et al., 2009; Duong et al., 2011; Terai et al.,  
816 2012; Jung et al., 2016; Gupta et al., 2022).

817 The investigations of the ACI via the  $ACI_{N, CB}$  and  $ACI_{r, CB}$  indices reveal that during the ACE-  
818 ENA wintertime,  $N_c$  is more sensitive to changes in  $N_{CCN0.35\%}$ , indicating aerosols more readily activate  
819 to become cloud droplets compared to those in the summer, which is consistent with the previous  
820 assessment by J. Wang et al. (2022) on the seasonal dependency of the relationship between  $N_c$  and  
821 aerosols. One influencing factor is the strong dynamic mechanism that speeds up the infusion of CCN  
822 into the cloud layer, thus aiding droplet formation. The moderate but statistically significant correlation  
823 coefficients between the CCN activation fractions and the TKE agree with a previous study that found  
824 the local activation fraction of CCN to be strongly associated with increased updrafts (Hu et al., 2021).  
825 Furthermore, the presence of larger aerosols during ACE-ENA winter enhances the droplet activation

826 process. The SOCRATES IOP highlights a higher  $ACI_{r, CB}$ , indicating a pronounced decrease in  $r_c$  with  
827 increasing  $N_{CCN0.35\%}$ . The  $ACI_{r, CB}$  in ACE-ENA is dampened by the presence of more large cloud  
828 droplets near the cloud base, particularly under relatively higher  $N_{CCN0.35\%}$ . However, the combined  
829 effect of the relatively cleaner environment and sufficient water vapor results in stronger cloud  
830 microphysical responses during the ACE-ENA wintertime than in the summertime. Note that the ACI  
831 indices from this study lie in the higher end of the ACI ranges estimated via remote sensing (McComiskey  
832 et al., 2009; Dong et al., 2015; Zheng et al., 2022a) possibly because the aircraft assessment of ACI is  
833 based on measurements where the aerosols are in direct contact with the cloud layer. Arguably, the  
834 assessment of  $N_c$  responses to  $N_{CCN0.35\%}$  would inevitably be affected by the collision-coalescence  
835 process near the cloud base, where simultaneously, the CCN replenishment buffers the  $N_c$  and the  
836 collision-coalescence process depletes  $N_c$ . Hence, finding a layer where these two effects maintain a  
837 dynamic balance in  $N_c$  might aid in a more accurate assessment and more fundamental understanding of  
838 the ACI, which might be revealed by the LES or parcel model simulations.

839 Additionally, the in-cloud drizzle formation and evolution processes significantly influence the  
840 sub-cloud CCN budgets via the coalescence-scavenging effect, which can potentially exaggerate the  
841 assessment of cloud microphysics susceptibilities. Based on the CCN loss rate ( $L_{CCN}$ ) from ACE-ENA  
842 and SOCRATES, a sensitivity analysis is performed focusing on retrospectively adjusting the sub-cloud  
843 CCN according to their  $L_{CCN}$ . Results showed that this adjustment led to a decreased  $ACI_{r, CB}$ ,  
844 highlighting the significance of the coalescence-scavenging process on the ACI assessment. However,  
845 due to the fact that aircraft only provide a snapshot of the clouds and aerosol information, determining  
846 the precise drizzle timing for the individual cloud is challenging. Hence, findings from this retrospective  
847 approach provide only a direction or theory, and should be taken cautiously. Nevertheless, pursuing  
848 further modeling experiments on this matter may be worthwhile. For example, the exact drizzling time  
849 could be pinpointed within a model using an Eulerian framework or traced using a Lagrangian framework.

850 Nevertheless, the CCN adjustment could more accurately reflect the true characteristics of the cloud and  
851 the MBL CCN budget, potentially aiding in a more precise assessment of ACI. Therefore, future works  
852 would focus on the model simulation on the MBL clouds from ACE-ENA and SOCRATES and further  
853 assess the modeled ACI under the observational constraints, as well as the continuous development of  
854 the warm rain microphysical parameterizations, in order to aid in the better represent the MBL clouds in  
855 multiple regions.

856

857

858 *Data availability.* The ACE-ENA field campaign data can be accessed from the Department of Energy  
859 Atmospheric Radiation Measurement data archive ([https://iop.archive.arm.gov/arm-iop-](https://iop.archive.arm.gov/arm-iop-file/2017/ena/aceena/)  
860 [file/2017/ena/aceena/](https://iop.archive.arm.gov/arm-iop-file/2017/ena/aceena/)). The SOCRATES field campaign data are publicly archived on the National  
861 Center for Atmospheric Research (NCAR) Earth Observing Laboratory  
862 ([https://data.eol.ucar.edu/master\\_lists/generated/socrates/](https://data.eol.ucar.edu/master_lists/generated/socrates/)).

863

864 *Author contributions.* The original idea of this study is discussed by XZ, XD, and BX. XZ performed the  
865 analyses and wrote the manuscript. XZ, XD, BX, TL, and YW participated in further scientific  
866 discussions and provided substantial comments and edits on the paper.

867

868 *Competing interests.* At least one of the (co-)authors is a member of the editorial board of Atmospheric  
869 Chemistry and Physics.

870

871 *Acknowledgments.* This work was supported by the NSF grants AGS-2031750/2031751/20211752 at the  
872 University of Arizona, Texas A&M University and Stanford University, respectively. The authors  
873 sincerely thank the investigators and mentors from the ACE-ENA and SOCRATES field campaigns for  
874 making the data publicly available.

875 **References.**

- 876 Albrecht B. A.: Aerosols, Cloud Microphysics, and Fractional Cloudiness, *Science*, 245, 1227-1230,  
877 10.1126/science.245.4923.1227, 1989
- 878 Albrecht, B. A., Bretherton, C. S., Johnson, D., Scubert, W. H., and Frisch, A. S.: The Atlantic  
879 Stratocumulus Transition Experiment—ASTEX, *B. Am. Meteorol. Soc.*, 76, 889-904,  
880 10.1175/1520-0477(1995)076<0889:Taste>2.0.Co;2, 1995.
- 881 Albrecht, B., Fang, M., and Ghate, V.: Exploring Stratocumulus Cloud-Top Entrainment Processes and  
882 Parameterizations by Using Doppler Cloud Radar Observations, *J. Atmos. Sci.*, 73, 729-742,  
883 10.1175/JAS-D-15-0147.1, 2016.
- 884 Atlas, R. L., Bretherton, C. S., Blossey, P. N., Gettelman, A., Bardeen, C., Lin, P., and Ming, Y.: How  
885 Well Do Large-Eddy Simulations and Global Climate Models Represent Observed Boundary Layer  
886 Structures and Low Clouds Over the Summertime Southern Ocean?, *Journal of Advances in*  
887 *Modeling Earth Systems*, 12, e2020MS002205, <https://doi.org/10.1029/2020MS002205>, 2020.
- 888 Atlas, R., Mohrmann, J., Finlon, J., Lu, J., Hsiao, I., Wood, R., and Diao, M.: The University of  
889 Washington Ice–Liquid Discriminator (UWILD) improves single-particle phase classifications of  
890 hydrometeors within Southern Ocean clouds using machine learning, *Atmos. Meas. Tech.*, 14,  
891 7079-7101, 10.5194/amt-14-7079-2021, 2021.
- 892 Baumgardner, D. and Korolev, A.: Airspeed Corrections for Optical Array Probe Sample Volumes, *J.*  
893 *Atmos. Ocean. Tech.*, 14, 1224-1229, [https://doi.org/10.1175/1520-](https://doi.org/10.1175/1520-0426(1997)014<1224:ACFOAP>2.0.CO;2)  
894 [0426\(1997\)014<1224:ACFOAP>2.0.CO;2](https://doi.org/10.1175/1520-0426(1997)014<1224:ACFOAP>2.0.CO;2), 1997.
- 895 Baumgardner, D., Abel, S. J., Axisa, D., Cotton, R., Crosier, J., Field, P., Gurganus, C., Heymsfield, A.,  
896 Korolev, A., Krämer, M., Lawson, P., McFarquhar, G., Ulanowski, Z., and Um, J.: Cloud Ice  
897 Properties: In Situ Measurement Challenges, *Meteor. Monogr.*, 58, 9.1-9.23,  
898 <https://doi.org/10.1175/AMSMONOGRAPHS-D-16-0011.1>, 2017.

899 Braun, R. A., Dadashazar, H., MacDonald, A. B., Crosbie, E., Jonsson, H. H., Woods, R. K., Flagan, R.  
900 C., Seinfeld, J. H., and Sorooshian, A.: Cloud Adiabaticity and Its Relationship to Marine  
901 Stratocumulus Characteristics Over the Northeast Pacific Ocean, *J. Geophys. Res.-Atmos.*, 123,  
902 13790 - 13806, [10.1029/2018jd029287](https://doi.org/10.1029/2018jd029287), 2018.

903 Brenguier, J. L., Burnet, F., and Geoffroy, O.: Cloud optical thickness and liquid water path – does the k  
904 coefficient vary with droplet concentration?, *Atmos. Chem. Phys.*, 11, 9771-9786, [10.5194/acp-11-](https://doi.org/10.5194/acp-11-9771-2011)  
905 [9771-2011](https://doi.org/10.5194/acp-11-9771-2011), 2011.

906 Brost, R. A., Wyngaard, J. C., and Lenschow, D. H.: Marine Stratocumulus Layers. Part II: Turbulence  
907 Budgets, *J. Atmos. Sci.*, 39, 818-836, [10.1175/1520-0469\(1982\)039<0818:MSLPIT>2.0.CO;2](https://doi.org/10.1175/1520-0469(1982)039<0818:MSLPIT>2.0.CO;2),  
908 1982.

909 Brunke, M. A., Cutler, L., Urzua, R. D., Corral, A. F., Crosbie, E., Hair, J., Hostetler, C., Kirschler, S.,  
910 Larson, V., Li, X.-Y., Ma, P.-L., Minke, A., Moore, R., Robinson, C. E., Scarino, A. J., Schlosser,  
911 J., Shook, M., Sorooshian, A., Lee Thornhill, K., Voigt, C., Wan, H., Wang, H., Winstead, E., Zeng,  
912 X., Zhang, S., and Ziemba, L. D.: Aircraft Observations of Turbulence in Cloudy and Cloud-Free  
913 Boundary Layers Over the Western North Atlantic Ocean From ACTIVATE and Implications for  
914 the Earth System Model Evaluation and Development, *J. Geophys. Res.-Atmos.*, 127,  
915 [e2022JD036480](https://doi.org/10.1029/2022JD036480), <https://doi.org/10.1029/2022JD036480>, 2022.

916 Chen, J., Liu, Y., Zhang, M., and Peng, Y.: Height Dependency of Aerosol-Cloud Interaction Regimes,  
917 *J. Geophys. Res.-Atmos.*, 123, 491-506, <https://doi.org/10.1002/2017JD027431>, 2018.

918 Chen, S., Yau, M. K., and Bartello, P.: Turbulence Effects of Collision Efficiency and Broadening of  
919 Droplet Size Distribution in Cumulus Clouds, *J. Atmos. Sci.*, 75, 203-217,  
920 <https://doi.org/10.1175/JAS-D-17-0123.1>, 2018.

921 Chen, Y. C., Xue, L., Lebo, Z. J., Wang, H., Rasmussen, R. M., and Seinfeld, J. H.: A comprehensive  
922 numerical study of aerosol-cloud-precipitation interactions in marine stratocumulus, *Atmos. Chem.*  
923 *Phys.*, 11, 9749-9769, [10.5194/acp-11-9749-2011](https://doi.org/10.5194/acp-11-9749-2011), 2011.

924 Christensen, M. W., Ma, P. L., Wu, P., Varble, A. C., Mülmenstädt, J., and Fast, J. D.: Evaluation of  
925 aerosol–cloud interactions in E3SM using a Lagrangian framework, *Atmos. Chem. Phys.*, 23, 2789-  
926 2812, 10.5194/acp-23-2789-2023, 2023.

927 Comstock, K. K., Wood, R., Yuter, S. E., and Bretherton, C. S.: Reflectivity and rain rate in and below  
928 drizzling stratocumulus, *Q. J. R. Meteor. Soc.*, 130, 2891-2918, <https://doi.org/10.1256/qj.03.187>,  
929 2004.

930 Cooper, W. A., Friesen, R. B., Hayman, M., Jensen, J., Lenschow, D. H., Romashkin, P., Schanot, A., Spuler, S.,  
931 Stith, J., and Wolff, C.: Characterization of Uncertainty in Measurements of Wind from the NSF/NCAR  
932 Gulfstream V Research Aircraft (No. NCAR/TN-528+STR), NCAR Technical Notes,  
933 doi:10.5065/D60G3HJ8, 2016.

934 Covert, D. S., Kapustin, V. N., Bates, T. S., and Quinn, P. K.: Physical properties of marine boundary  
935 layer aerosol particles of the mid-Pacific in relation to sources and meteorological transport, *J.*  
936 *Geophys. Res.-Atmos.*, 101, 6919-6930, <https://doi.org/10.1029/95JD03068>, 1996.

937 D'Alessandro, J. J., McFarquhar, G. M., Wu, W., Stith, J. L., Jensen, J. B., and Rauber, R. M.:  
938 Characterizing the Occurrence and Spatial Heterogeneity of Liquid, Ice, and Mixed Phase Low-  
939 Level Clouds Over the Southern Ocean Using in Situ Observations Acquired During SOCRATES,  
940 *J. Geophys. Res.-Atmos.*, 126, e2020JD034482, <https://doi.org/10.1029/2020JD034482>, 2021.

941 Danker, J., Sourdeval, O., McCoy, I. L., Wood, R., and Possner, A.: Exploring relations between cloud  
942 morphology, cloud phase, and cloud radiative properties in Southern Ocean's stratocumulus clouds,  
943 *Atmos. Chem. Phys.*, 22, 10247-10265, 10.5194/acp-22-10247-2022, 2022.

944 Desai, N., Liu, Y., Glienke, S., Shaw, R. A., Lu, C., Wang, J., and Gao, S.: Vertical Variation of Turbulent  
945 Entrainment Mixing Processes in Marine Stratocumulus Clouds Using High-Resolution Digital  
946 Holography, *J. Geophys. Res.-Atmos.*, 126, e2020JD033527,  
947 <https://doi.org/10.1029/2020JD033527>, 2021.

948 Dong, X., Schwantes, A. C., Xi, B., and Wu, P.: Investigation of the marine boundary layer cloud and  
949 CCN properties under coupled and decoupled conditions over the Azores, *J. Geophys. Res.-Atmos.*,  
950 120, 6179-6191, <https://doi.org/10.1002/2014JD022939>, 2015.

951 Dong, X., X. Zheng, B. Xi, and S. Xie (2023), A Climatology of Midlatitude Maritime Cloud Fraction  
952 and Radiative Effect Derived from the ARM ENA Ground-Based Observations, *J. Climate*, 36(2),  
953 531-546, doi:10.1175/JCLI-D-22-0290.1.

954 Duong, H. T., Sorooshian, A., and Feingold, G.: Investigating potential biases in observed and modeled  
955 metrics of aerosol-cloud-precipitation interactions, *Atmos. Chem. Phys.*, 11, 4027-4037,  
956 10.5194/acp-11-4027-2011, 2011.

957 Fan, C., Wang, M., Rosenfeld, D., Zhu, Y., Liu, J., and Chen, B.: Strong Precipitation Suppression by  
958 Aerosols in Marine Low Clouds, *Geophys. Res. Lett.*, 47, e2019GL086207,  
959 <https://doi.org/10.1029/2019GL086207>, 2020.

960 Feingold, G., Frisch, A. S., Stevens, B., and Cotton, W. R.: On the relationship among cloud turbulence,  
961 droplet formation and drizzle as viewed by Doppler radar, microwave radiometer and lidar, *J.*  
962 *Geophys. Res.-Atmos.*, 104, 22195-22203, <https://doi.org/10.1029/1999JD900482>, 1999.

963 Feingold, G., Kreidenweis, S. M., Stevens, B., and Cotton, W. R.: Numerical simulations of  
964 stratocumulus processing of cloud condensation nuclei through collision-coalescence, *J. Geophys.*  
965 *Res.-Atmos.*, 101, 21391-21402, <https://doi.org/10.1029/96JD01552>, 1996.

966 Feingold, G. and McComiskey, A.: ARM's Aerosol-Cloud-Precipitation Research (Aerosol Indirect Effects),  
967 *Meteor. Monogr.*, 57, 22.21-22.15, 10.1175/AMSMONOGRAPHS-D-15-0022.1, 2016.

968 Feingold, G. and Siebert, H.: Cloud – Aerosol Interactions from the Micro to the Cloud Scale, from the  
969 Strungmann Forum Report, Clouds in the Perturbed Climate System: Their Relationship to Energy  
970 Balance, Atmospheric Dynamics, and Precipitation, 2, edited by: Heintzenberg, J. and Charlson, R.  
971 J., MIT Press, ISBN 978-0-262-01287-4, 2009.



972 Flossmann, A. I., Hall, W. D., and Pruppacher, H. R.: A Theoretical Study of the Wet Removal of  
973 Atmospheric Pollutants. Part I: The Redistribution of Aerosol Particles Captured through  
974 Nucleation and Impaction Scavenging by Growing Cloud Drops, *J. Atmos. Sci.*, 42, 583-606,  
975 [https://doi.org/10.1175/1520-0469\(1985\)042<0583:ATSOTW>2.0.CO;2](https://doi.org/10.1175/1520-0469(1985)042<0583:ATSOTW>2.0.CO;2), 1985.

976 Gao, S., Lu, C., Liu, Y., Mei, F., Wang, J., Zhu, L., and Yan, S.: Contrasting Scale Dependence of  
977 Entrainment-Mixing Mechanisms in Stratocumulus Clouds, *Geophys. Res. Lett.*, 47,  
978 e2020GL086970, <https://doi.org/10.1029/2020GL086970>, 2020.

979 Ghate, V. P. and Cadeddu, M. P.: Drizzle and Turbulence Below Closed Cellular Marine Stratocumulus  
980 Clouds, *J. Geophys. Res.-Atmos.*, 124, 5724-5737, <https://doi.org/10.1029/2018JD030141>, 2019.

981 Ghate, V. P., Cadeddu, M. P., Zheng, X., and O'Connor, E.: Turbulence in the Marine Boundary Layer  
982 and Air Motions below Stratocumulus Clouds at the ARM Eastern North Atlantic Site, *J. Appl.*  
983 *Meteorol. Clim.*, 60, 1495-1510, 10.1175/JAMC-D-21-0087.1, 2021.

984 Grabowski, W. W. and Wang, L.-P.: Growth of Cloud Droplets in a Turbulent Environment, *Annual*  
985 *Review of Fluid Mechanics*, 45, 293-324, 10.1146/annurev-fluid-011212-140750, 2013.

986 Grosvenor, D. P., Sourdeval, O., Zuidema, P., Ackerman, A., Alexandrov, M. D., Bennartz, R., Boers,  
987 R., Cairns, B., Chiu, J. C., Christensen, M., Deneke, H., Diamond, M., Feingold, G., Fridlind, A.,  
988 Hünerbein, A., Knist, C., Kollias, P., Marshak, A., McCoy, D., Merk, D., Painemal, D., Rausch, J.,  
989 Rosenfeld, D., Russchenberg, H., Seifert, P., Sinclair, K., Stier, P., van Dierenhoven, B., Wendisch,  
990 M., Werner, F., Wood, R., Zhang, Z., and Quaas, J.: Remote Sensing of Droplet Number  
991 Concentration in Warm Clouds: A Review of the Current State of Knowledge and Perspectives,  
992 *Reviews of Geophysics*, 56, 409-453, <https://doi.org/10.1029/2017RG000593>, 2018.

993 Gupta, S., McFarquhar, G. M., O'Brien, J. R., Delene, D. J., Poellot, M. R., Dobracki, A., Podolske, J.  
994 R., Redemann, J., LeBlanc, S. E., Segal-Rozenhaimer, M., and Pistone, K.: Impact of the variability  
995 in vertical separation between biomass burning aerosols and marine stratocumulus on cloud

996 microphysical properties over the Southeast Atlantic, *Atmos. Chem. Phys.*, 21, 4615– 4635,  
997 <https://doi.org/10.5194/acp-21-4615-2021>, 2021.

998 Gupta, S., McFarquhar, G. M., O'Brien, J. R., Poellot, M. R., Delene, D. J., Miller, R. M., and Small  
999 Griswold, J. D.: Factors affecting precipitation formation and precipitation susceptibility of marine  
1000 stratocumulus with variable above- and below-cloud aerosol concentrations over the Southeast  
1001 Atlantic, *Atmos. Chem. Phys.*, 22, 2769–2793, <https://doi.org/10.5194/acp-22-2769-2022>, 2022.

1002 Hansen, J. E. and Travis, L. D.: Light scattering in planetary atmospheres, *Space Sci. Rev.*, 16, 527-610,  
1003 [doi:10.1007/BF00168069](https://doi.org/10.1007/BF00168069), 1974.

1004 Hill, A. A., Feingold, G., and Jiang, H.: The Influence of Entrainment and Mixing Assumption on  
1005 Aerosol–Cloud Interactions in Marine Stratocumulus, *J. Atmos. Sci.*, 66, 1450-1464,  
1006 [10.1175/2008JAS2909.1](https://doi.org/10.1175/2008JAS2909.1), 2009.

1007 Hinds, W.C.: *Aerosol Technology, Properties, Behaviour, and Measurement of Airborne Particles*. John  
1008 Wiley & Sons Inc., New York., 1999.

1009 Hoffmann, F. and Feingold, G.: A Note on Aerosol Processing by Droplet Collision-Coalescence,  
1010 *Geophys. Res. Lett.*, 50, e2023GL103716, <https://doi.org/10.1029/2023GL103716>, 2023.

1011 Hu, A. Z., Igel, A. L., Chuang, P. Y., and Witte, M. K.: Recognition of Inter-Cloud Versus Intra-Cloud  
1012 Controls on Droplet Dispersion With Applications to Microphysics Parameterization, *J. Geophys.*  
1013 *Res.-Atmos.*, 126, e2021JD035180, <https://doi.org/10.1029/2021JD035180>, 2021.

1014 Hudson, J. G. and Noble, S.: CCN Spectral Shape and Cumulus Cloud and Drizzle Microphysics, *J.*  
1015 *Geophys. Res.-Atmos.*, 125, e2019JD031141, <https://doi.org/10.1029/2019JD031141>, 2020.

1016 Jensen, M. P., Ghatge, V. P., Wang, D., Apoznanski, D. K., Bartholomew, M. J., Giangrande, S. E.,  
1017 Johnson, K. L., and Thieman, M. M.: Contrasting characteristics of open- and closed-cellular  
1018 stratocumulus cloud in the eastern North Atlantic, *Atmos. Chem. Phys.*, 21, 14557-14571,  
1019 [10.5194/acp-21-14557-2021](https://doi.org/10.5194/acp-21-14557-2021), 2021.

1020 Jones, C. R., Bretherton, C. S., and Leon, D.: Coupled vs. decoupled boundary layers in VOCALS-REx,  
1021 Atmos. Chem. Phys., 11, 7143-7153, 10.5194/acp-11-7143-2011, 2011.

1022 Jung, E., Albrecht, B. A., Sorooshian, A., Zuidema, P., and Jonsson, H. H.: Precipitation susceptibility  
1023 in marine stratocumulus and shallow cumulus from airborne measurements, Atmos. Chem. Phys.,  
1024 16, 11395-11413, 10.5194/acp-16-11395-2016, 2016.

1025 Kang, L., Marchand, R. T., Wood, R., and McCoy, I. L.: Coalescence Scavenging Drives Droplet  
1026 Number Concentration in Southern Ocean Low Clouds, Geophys. Res. Lett., 49, e2022GL097819,  
1027 <https://doi.org/10.1029/2022GL097819>, 2022.

1028 Kang, L., Marchand, R. T., and Wood, R.: Stratocumulus Precipitation Properties Over the Southern  
1029 Ocean Observed From Aircraft During the SOCRATES Campaign, J. Geophys. Res.-Atmos., 129,  
1030 e2023JD039831, <https://doi.org/10.1029/2023JD039831>, 2024.

1031 Kim, S. H., Kim, J., Kim, J. H., and Chun, H. Y.: Characteristics of the derived energy dissipation rate  
1032 using the 1&thinsp;Hz commercial aircraft quick access recorder (QAR) data, Atmos. Meas. Tech.,  
1033 15, 2277-2298, 10.5194/amt-15-2277-2022, 2022.

1034 Lang, F., Ackermann, L., Huang, Y., Truong, S. C. H., Siems, S. T., and Manton, M. J.: A climatology  
1035 of open and closed mesoscale cellular convection over the Southern Ocean derived from Himawari-  
1036 8 observations, Atmos. Chem. Phys., 22, 2135-2152, 10.5194/acp-22-2135-2022, 2022.

1037 Lu, C., Zhu, L., Liu, Y., Mei, F., Fast, J. D., Pekour, M. S., Luo, S., Xu, X., He, X., Li, J., and Gao, S.:  
1038 Observational study of relationships between entrainment rate, homogeneity of mixing, and cloud  
1039 droplet relative dispersion, Atmos. Res., 293, 106900,  
1040 <https://doi.org/10.1016/j.atmosres.2023.106900>, 2023.

1041 Lu, M.-L., Sorooshian, A., Jonsson, H. H., Feingold, G., Flagan, R. C., and Seinfeld, J. H.: Marine  
1042 stratocumulus aerosol-cloud relationships in the MASE-II experiment: Precipitation susceptibility  
1043 in eastern Pacific marine stratocumulus, J. Geophys. Res.-Atmos., 114,  
1044 <https://doi.org/10.1029/2009JD012774>, 2009.

1045 Mann, J. A. L., Christine Chiu, J., Hogan, R. J., O'Connor, E. J., L'Ecuyer, T. S., Stein, T. H. M., and  
1046 Jefferson, A.: Aerosol impacts on drizzle properties in warm clouds from ARM Mobile Facility  
1047 maritime and continental deployments, *J. Geophys. Res.-Atmos.*, 119, 4136-4148,  
1048 <https://doi.org/10.1002/2013JD021339>, 2014.

1049 Marcovecchio, A. R., Xi, B., Zheng, X., Wu, P., Dong, X., and Behrangi, A.: What Are the Similarities  
1050 and Differences in Marine Boundary Layer Cloud and Drizzle Microphysical Properties During the  
1051 ACE-ENA and MARCUS Field Campaigns?, *J. Geophys. Res.-Atmos.*, 128, e2022JD037109,  
1052 <https://doi.org/10.1029/2022JD037109>, 2023.

1053 Mechem, D. B., Wittman, C. S., Miller, M. A., Yuter, S. E., and de Szoeke, S. P.: Joint Synoptic and  
1054 Cloud Variability over the Northeast Atlantic near the Azores, *J. Appl. Meteorol. Clim.*, 57, 1273-  
1055 1290, <https://doi.org/10.1175/JAMC-D-17-0211.1>, 2018.

1056 McComiskey, A., Feingold, G., Frisch, A. S., Turner, D. D., Miller, M. A., Chiu, J. C., Min, Q., and  
1057 Ogren, J. A.: An assessment of aerosol-cloud interactions in marine stratus clouds based on surface  
1058 remote sensing, *J. Geophys. Res.-Atmos.*, 114, <https://doi.org/10.1029/2008JD011006>, 2009.

1059 McCoy, I. L., Wood, R., and Fletcher, J. K.: Identifying Meteorological Controls on Open and Closed  
1060 Mesoscale Cellular Convection Associated with Marine Cold Air Outbreaks, *J. Geophys. Res.-*  
1061 *Atmos.*, 122, 11,678-611,702, <https://doi.org/10.1002/2017JD027031>, 2017.

1062 McCoy, I. L., McCoy, D. T., Wood, R., Regayre, L., Watson-Parris, D., Grosvenor, D. P., Mulcahy, J.  
1063 P., Hu, Y., Bender, F. A. M., Field, P. R., Carslaw, K. S., and Gordon, H.: The hemispheric contrast  
1064 in cloud microphysical properties constrains aerosol forcing, *P. Natl. Acad. Sci. USA*, 117, 18998-  
1065 19006, [10.1073/pnas.1922502117](https://doi.org/10.1073/pnas.1922502117), 2020.

1066 McCoy, I. L., Bretherton, C. S., Wood, R., Twohy, C. H., Gettelman, A., Bardeen, C. G., and Toohey,  
1067 D. W.: Influences of Recent Particle Formation on Southern Ocean Aerosol Variability and Low  
1068 Cloud Properties, *J. Geophys. Res.-Atmos.*, 126, e2020JD033529,  
1069 <https://doi.org/10.1029/2020JD033529>, 2021.

1070 McFarquhar, G. M., Bretherton, C. S., Marchand, R., Protat, A., DeMott, P. J., Alexander, S. P., Roberts,  
1071 G. C., Twohy, C. H., Toohey, D., Siems, S., Huang, Y., Wood, R., Rauber, R. M., Lasher-Trapp,  
1072 S., Jensen, J., Stith, J. L., Mace, J., Um, J., Järvinen, E., Schnaiter, M., Gettelman, A., Sanchez, K.  
1073 J., McCluskey, C. S., Russell, L. M., McCoy, I. L., Atlas, R. L., Bardeen, C. G., Moore, K. A., Hill,  
1074 T. C. J., Humphries, R. S., Keywood, M. D., Ristovski, Z., Cravigan, L., Schofield, R., Fairall, C.,  
1075 Mallet, M. D., Kreidenweis, S. M., Rainwater, B., D'Alessandro, J., Wang, Y., Wu, W., Saliba, G.,  
1076 Levin, E. J. T., Ding, S., Lang, F., Truong, S. C. H., Wolff, C., Haggerty, J., Harvey, M. J.,  
1077 Klekociuk, A. R., and McDonald, A.: Observations of Clouds, Aerosols, Precipitation, and Surface  
1078 Radiation over the Southern Ocean: An Overview of CAPRICORN, MARCUS, MICRE, and  
1079 SOCRATES, *B. Am. Meteorol. Soc.*, 102, E894-E928, [https://doi.org/10.1175/BAMS-D-20-](https://doi.org/10.1175/BAMS-D-20-0132.1)  
1080 0132.1, 2021.

1081 Muñoz-Esparza, D., Sharman, R. D., and Lundquist, J. K.: Turbulence Dissipation Rate in the  
1082 Atmospheric Boundary Layer: Observations and WRF Mesoscale Modeling during the XPIA Field  
1083 Campaign, *Mon. Weather Rev.*, 146, 351-371, <https://doi.org/10.1175/MWR-D-17-0186.1>, 2018.

1084 Olfert, J. S., Kulkarni, P., and Wang, J.: Measuring aerosol size distributions with the fast integrated  
1085 mobility spectrometer, *Journal of Aerosol Science*, 39, 940-956,  
1086 <https://doi.org/10.1016/j.jaerosci.2008.06.005>, 2008.

1087 Painemal, D. and Zuidema, P.: Assessment of MODIS cloud effective radius and optical thickness  
1088 retrievals over the Southeast Pacific with VOCALS-REx in situ measurements, *J. Geophys. Res.-*  
1089 *Atmos.*, 116, <https://doi.org/10.1029/2011JD016155>, 2011.

1090 Painemal, D., Chang, F. L., Ferrare, R., Burton, S., Li, Z., Smith Jr, W. L., Minnis, P., Feng, Y., and  
1091 Clayton, M.: Reducing uncertainties in satellite estimates of aerosol–cloud interactions over the  
1092 subtropical ocean by integrating vertically resolved aerosol observations, *Atmos. Chem. Phys.*, 20,  
1093 7167-7177, [10.5194/acp-20-7167-2020](https://doi.org/10.5194/acp-20-7167-2020), 2020.

1094 Painemal, D., Spangenberg, D., Smith Jr, W. L., Minnis, P., Cairns, B., Moore, R. H., Crosbie, E.,  
1095 Robinson, C., Thornhill, K. L., Winstead, E. L., and Ziemba, L.: Evaluation of satellite retrievals of  
1096 liquid clouds from the GOES-13 imager and MODIS over the midlatitude North Atlantic during the  
1097 NAAMES campaign, *Atmos. Meas. Tech.*, 14, 6633-6646, 10.5194/amt-14-6633-2021, 2021.

1098 Pinsky, M. B. and Khain, A. P.: Turbulence effects on droplet growth and size distribution in clouds—  
1099 A review, *Journal of Aerosol Science*, 28, 1177-1214, [https://doi.org/10.1016/S0021-](https://doi.org/10.1016/S0021-8502(97)00005-0)  
1100 8502(97)00005-0, 1997.

1101 Pruppacher, H. R. and Klett, J. D.: *Microphysics of clouds and precipitation*, Kluwer Academic  
1102 Publishers, Dordrecht, the Netherlands, 1997.

1103 Rémillard, J. and Tselioudis, G.: Cloud Regime Variability over the Azores and Its Application to  
1104 Climate Model Evaluation, *J. Climate*, 28, 9707-9720, <https://doi.org/10.1175/JCLI-D-15-0066.1>,  
1105 2015.

1106 Sanchez, K. J., Roberts, G. C., Diao, M., and Russell, L. M.: Measured Constraints on Cloud Top  
1107 Entrainment to Reduce Uncertainty of Nonprecipitating Stratocumulus Shortwave Radiative  
1108 Forcing in the Southern Ocean, *Geophys. Res. Lett.*, 47, e2020GL090513,  
1109 <https://doi.org/10.1029/2020GL090513>, 2020.

1110 Sanchez, K. J., Roberts, G. C., Saliba, G., Russell, L. M., Twohy, C., Reeves, J. M., Humphries, R. S.,  
1111 Keywood, M. D., Ward, J. P., and McRobert, I. M.: Measurement report: Cloud processes and the  
1112 transport of biological emissions affect southern ocean particle and cloud condensation nuclei  
1113 concentrations, *Atmos. Chem. Phys.*, 21, 3427-3446, 10.5194/acp-21-3427-2021, 2021.

1114 Siebert, H., Shaw, R. A., and Warhaft, Z.: Statistics of Small-Scale Velocity Fluctuations and Internal  
1115 Intermittency in Marine Stratocumulus Clouds, *J. Atmos. Sci.*, 67, 262-273,  
1116 <https://doi.org/10.1175/2009JAS3200.1>, 2010.

1117 Smalley, M. A., Witte, M. K., Jeong, J.-H., and Chinita, M. J.: A climatology of cold pools distinct from  
1118 background turbulence at the Eastern North Atlantic observations site, EGU sphere [preprint],  
1119 <https://doi.org/10.5194/egusphere-2024-1098>, 2024.

1120 Stevens, B. and Feingold, G.: Untangling aerosol effects on clouds and precipitation in a buffered system,  
1121 *Nature*, 461, 607-613, [10.1038/nature08281](https://doi.org/10.1038/nature08281), 2009.

1122 Sorooshian, A., Feingold, G., Lebsock, M. D., Jiang, H., and Stephens, G. L.: On the precipitation  
1123 susceptibility of clouds to aerosol perturbations, *Geophys. Res. Lett.*, 36,  
1124 <https://doi.org/10.1029/2009GL038993>, 2009.

1125 Su, T., Li, Z., Henao, N. R., Luan, Q., and Yu, F.: Constraining effects of aerosol-cloud interaction by  
1126 accounting for coupling between cloud and land surface, *Science Advances*, 10, ead15044,  
1127 [10.1126/sciadv.ad15044](https://doi.org/10.1126/sciadv.ad15044),

1128 Terai, C. R. and Wood, R.: Aircraft observations of cold pools under marine stratocumulus, *Atmos.*  
1129 *Chem. Phys.*, 13, 9899-9914, [10.5194/acp-13-9899-2013](https://doi.org/10.5194/acp-13-9899-2013), 2013.

1130 Terai, C. R., Wood, R., Leon, D. C., and Zuidema, P.: Does precipitation susceptibility vary with  
1131 increasing cloud thickness in marine stratocumulus?, *Atmos. Chem. Phys.*, 12, 4567-4583,  
1132 [10.5194/acp-12-4567-2012](https://doi.org/10.5194/acp-12-4567-2012), 2012.

1133 Twohy, C. H., Petters, M. D., Snider, J. R., Stevens, B., Tahnk, W., Wetzal, M., Russell, L., and Burnet,  
1134 F.: Evaluation of the aerosol indirect effect in marine stratocumulus clouds: Droplet number, size,  
1135 liquid water path, and radiative impact, *J. Geophys. Res.-Atmos.*, 110,  
1136 <https://doi.org/10.1029/2004JD005116>, 2005.

1137 vanZanten, M. C., Stevens, B., Vali, G., and Lenschow, D. H.: Observations of Drizzle in Nocturnal  
1138 Marine Stratocumulus, *J. Atmos. Sci.*, 62, 88-106, <https://doi.org/10.1175/JAS-3355.1>, 2005.

1139 Wacławczyk, M., Ma, Y. F., Kopeć, J. M., and Malinowski, S. P.: Novel approaches to estimating the  
1140 turbulent kinetic energy dissipation rate from low- and moderate-resolution velocity fluctuation  
1141 time series, *Atmos. Meas. Tech.*, 10, 4573-4585, [10.5194/amt-10-4573-2017](https://doi.org/10.5194/amt-10-4573-2017), 2017.

1142 Wang, J., Wood, R., Jensen, M. P., Chiu, J. C., Liu, Y., Lamer, K., Desai, N., Giangrande, S. E., Knopf,  
1143 D. A., Kollias, P., Laskin, A., Liu, X., Lu, C., Mechem, D., Mei, F., Starzec, M., Tomlinson, J.,  
1144 Wang, Y., Yum, S. S., Zheng, G., Aiken, A. C., Azevedo, E. B., Blanchard, Y., China, S., Dong,  
1145 X., Gallo, F., Gao, S., Ghate, V. P., Glienke, S., Goldberger, L., Hardin, J. C., Kuang, C., Luke, E.  
1146 P., Matthews, A. A., Miller, M. A., Moffet, R., Pekour, M., Schmid, B., Sedlacek, A. J., Shaw, R.  
1147 A., Shilling, J. E., Sullivan, A., Suski, K., Veghte, D. P., Weber, R., Wyant, M., Yeom, J.,  
1148 Zawadowicz, M., and Zhang, Z.: Aerosol and Cloud Experiments in the Eastern North Atlantic  
1149 (ACE-ENA), *B. Am. Meteorol. Soc.*, 103, E619-E641, 10.1175/BAMS-D-19-0220.1, 2022.

1150 Wang, Y., Zhao, C., McFarquhar, G. M., Wu, W., Reeves, M., and Li, J.: Dispersion of Droplet Size  
1151 Distributions in Supercooled Non-precipitating Stratocumulus from Aircraft Observations Obtained  
1152 during the Southern Ocean Cloud Radiation Aerosol Transport Experimental Study, *J. Geophys.*  
1153 *Res.-Atmos.*, 126, e2020JD033720, <https://doi.org/10.1029/2020JD033720>, 2021a.

1154 Wang, Y., Zheng, G., Jensen, M. P., Knopf, D. A., Laskin, A., Matthews, A. A., Mechem, D., Mei, F.,  
1155 Moffet, R., Sedlacek, A. J., Shilling, J. E., Springston, S., Sullivan, A., Tomlinson, J., Veghte, D.,  
1156 Weber, R., Wood, R., Zawadowicz, M. A., and Wang, J.: Vertical profiles of trace gas and aerosol  
1157 properties over the eastern North Atlantic: variations with season and synoptic condition, *Atmos.*  
1158 *Chem. Phys.*, 21, 11079-11098, 10.5194/acp-21-11079-2021, 2021b.

1159 Wang, Y., Zheng, X., Dong, X., Xi, B., Wu, P., Logan, T., and Yung, Y. L.: Impacts of long-range  
1160 transport of aerosols on marine-boundary-layer clouds in the eastern North Atlantic, *Atmos. Chem.*  
1161 *Phys.*, 20, 14741-14755, 10.5194/acp-20-14741-2020, 2020.

1162 Wang, Y., Zheng, X., Dong, X., Xi, B., and Yung, Y. L.: Insights of warm-cloud biases in Community  
1163 Atmospheric Model 5 and 6 from the single-column modeling framework and Aerosol and Cloud  
1164 Experiments in the Eastern North Atlantic (ACE-ENA) observations, *Atmos. Chem. Phys.*, 23,  
1165 8591-8605, 10.5194/acp-23-8591-2023, 2023.



1166 Wallace, J. M. and Hobbs, P. V.: Atmospheric Science: An Introductory Survey, 2nd edn., Academic  
1167 Press/Elsevier, 483 pp, 2006.

1168 Witte, M. K., Chuang, P. Y., Ayala, O., Wang, L.-P., and Feingold, G.: Comparison of Observed and  
1169 Simulated Drop Size Distributions from Large-Eddy Simulations with Bin Microphysics, *Mon.  
1170 Weather Rev.*, 147, 477-493, <https://doi.org/10.1175/MWR-D-18-0242.1>, 2019.

1171 Wood, R.: Drizzle in Stratiform Boundary Layer Clouds. Part I: Vertical and Horizontal Structure, *J.  
1172 Atmos. Sci.*, 62, 3011-3033, 10.1175/JAS3529.1, 2005.

1173 Wood, R.: Rate of loss of cloud droplets by coalescence in warm clouds, *J. Geophys. Res.-Atmos.*, 111,  
1174 <https://doi.org/10.1029/2006JD007553>, 2006.

1175 Wood, R., Wyant, M., Bretherton, C. S., Rémillard, J., Kollias, P., Fletcher, J., Stemmler, J., de Szoeko,  
1176 S., Yuter, S., Miller, M., Mechem, D., Tselioudis, G., Chiu, J. C., Mann, J. A. L., O'Connor, E. J.,  
1177 Hogan, R. J., Dong, X., Miller, M., Ghate, V., Jefferson, A., Min, Q., Minnis, P., Palikonda, R.,  
1178 Albrecht, B., Luke, E., Hannay, C., and Lin, Y.: Clouds, Aerosols, and Precipitation in the Marine  
1179 Boundary Layer: An Arm Mobile Facility Deployment, *B. Am. Meteorol. Soc.*, 96, 419-440,  
1180 10.1175/BAMS-D-13-00180.1, 2015.

1181 Wu, P., Dong, X., and Xi, B.: A Climatology of Marine Boundary Layer Cloud and Drizzle Properties  
1182 Derived from Ground-Based Observations over the Azores, *J. Climate*, 33, 10133-10148,  
1183 10.1175/JCLI-D-20-0272.1, 2020.

1184 Wu, P., Dong, X., Xi, B., Liu, Y., Thieman, M., and Minnis, P.: Effects of environment forcing on marine  
1185 boundary layer cloud-drizzle processes, *J. Geophys. Res.-Atmos.*, 122, 4463-4478,  
1186 <https://doi.org/10.1002/2016JD026326>, 2017.

1187 Wyant, M. C., Bretherton, C. S., Wood, R., Blossey, P. N., and McCoy, I. L.: High Free-Tropospheric  
1188 Aitken-Mode Aerosol Concentrations Buffer Cloud Droplet Concentrations in Large-Eddy  
1189 Simulations of Precipitating Stratocumulus, *Journal of Advances in Modeling Earth Systems*, 14,  
1190 e2021MS002930, <https://doi.org/10.1029/2021MS002930>, 2022.

1191 Yeom, J. M., Yum, S. S., Shaw, R. A., La, I., Wang, J., Lu, C., Liu, Y., Mei, F., Schmid, B., and  
1192 Matthews, A.: Vertical Variations of Cloud Microphysical Relationships in Marine Stratocumulus  
1193 Clouds Observed During the ACE-ENA Campaign, *J. Geophys. Res.-Atmos.*, 126,  
1194 e2021JD034700, <https://doi.org/10.1029/2021JD034700>, 2021.

1195 Zawadowicz, M. A., Suski, K., Liu, J., Pekour, M., Fast, J., Mei, F., Sedlacek, A. J., Springston, S.,  
1196 Wang, Y., Zaveri, R. A., Wood, R., Wang, J., and Shilling, J. E.: Aircraft measurements of aerosol  
1197 and trace gas chemistry in the eastern North Atlantic, *Atmos. Chem. Phys.*, 21, 7983-8002,  
1198 10.5194/acp-21-7983-2021, 2021.

1199 Zhang, J., Zhou, X., Goren, T., and Feingold, G.: Albedo susceptibility of northeastern Pacific  
1200 stratocumulus: the role of covarying meteorological conditions, *Atmos. Chem. Phys.*, 22, 861-880,  
1201 10.5194/acp-22-861-2022, 2022.

1202 Zhang, X., Dong, X., Xi, B., and Zheng, X.: Aerosol Properties and Their Influences on Marine Boundary  
1203 Layer Cloud Condensation Nuclei over the Southern Ocean, *Atmosphere-Basel*, 14,  
1204 10.3390/atmos14081246, 2023.

1205 Zheng, G., Wang, Y., Aiken, A. C., Gallo, F., Jensen, M. P., Kollias, P., Kuang, C., Luke, E., Springston,  
1206 S., Uin, J., Wood, R., and Wang, J.: Marine boundary layer aerosol in the eastern North Atlantic:  
1207 seasonal variations and key controlling processes, *Atmos. Chem. Phys.*, 18, 17615-17635,  
1208 10.5194/acp-18-17615-2018, 2018.

1209 Zheng, G., Wang, Y., Wood, R., Jensen, M. P., Kuang, C., McCoy, I. L., Matthews, A., Mei, F.,  
1210 Tomlinson, J. M., Shilling, J. E., Zawadowicz, M. A., Crosbie, E., Moore, R., Ziemba, L., Andreae,  
1211 M. O., and Wang, J.: New particle formation in the remote marine boundary layer, *Nature*  
1212 *Communications*, 12, 527, 10.1038/s41467-020-20773-1, 2021.

1213 Zheng, X., Dong, X., Ward, D. M., Xi, B., Wu, P., and Wang, Y.: Aerosol-Cloud-Precipitation  
1214 Interactions in a Closed-cell and Non-homogenous MBL Stratocumulus Cloud, *Adv. Atmos. Sci.*,  
1215 39, 2107-2123, 10.1007/s00376-022-2013-6, 2022a.

1216 Zheng, X., Xi, B., Dong, X., Wu, P., Logan, T., and Wang, Y.: Environmental effects on aerosol–cloud  
1217 interaction in non-precipitating marine boundary layer (MBL) clouds over the eastern North  
1218 Atlantic, *Atmos. Chem. Phys.*, 22, 335-354, 10.5194/acp-22-335-2022, 2022b.

1219 Zuidema, P., Torri, G., Muller, C., and Chandra, A.: A Survey of Precipitation-Induced Atmospheric  
1220 Cold Pools over Oceans and Their Interactions with the Larger-Scale Environment, *Surveys in*  
1221 *Geophysics*, 38, 1283-1305, 10.1007/s10712-017-9447-x, 2017.

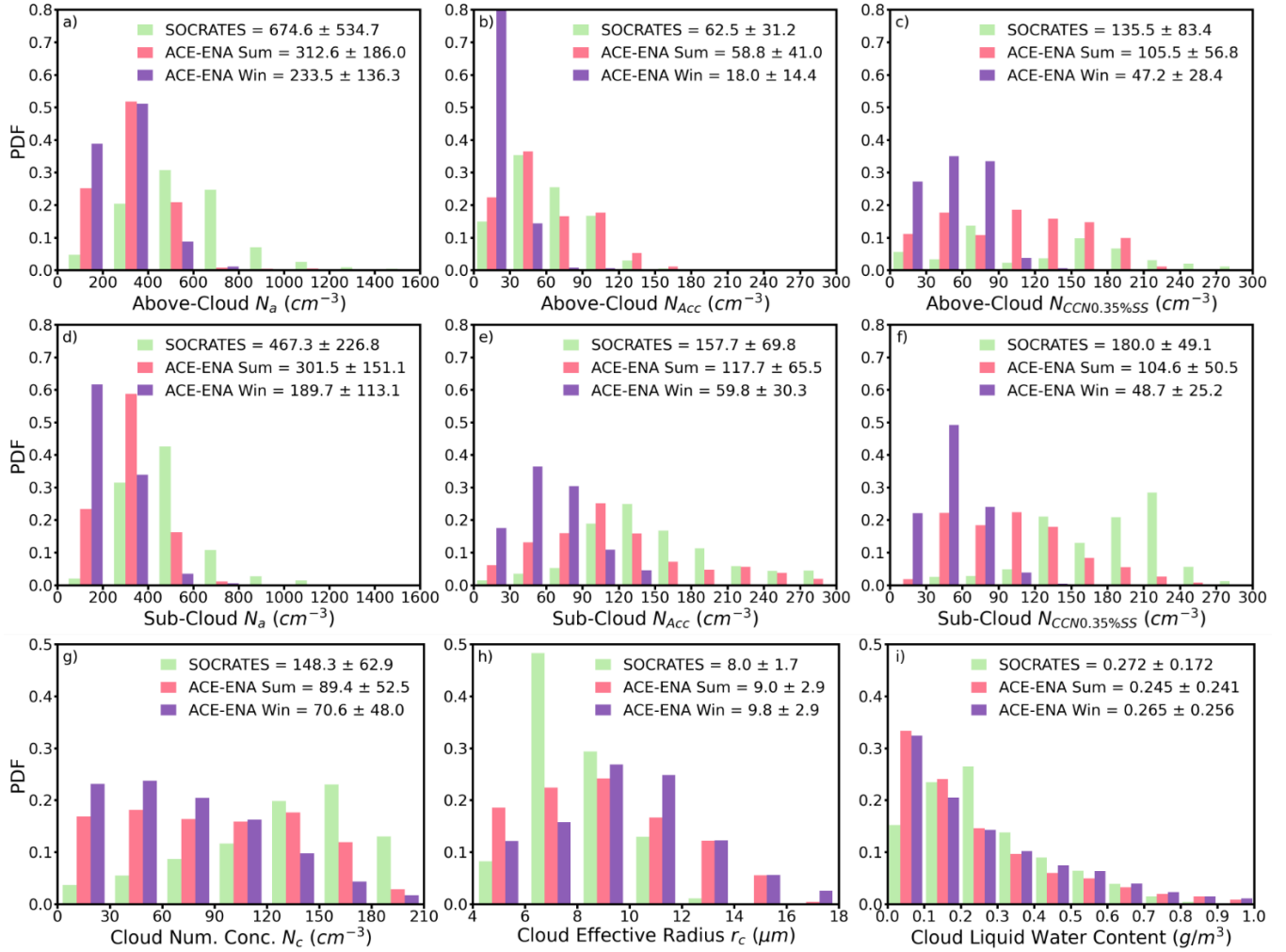


**Figure 1.** Probability Density Functions (PDFs) of  $N_a$ ,  $N_{ACC}$  and  $N_{CCN0.35\%}$  in the above-cloud (a, b, c) and sub-cloud (d, e, f) regimes; and the cloud microphysical properties of  $N_c$  (g),  $r_c$  (h), and  $LWC_c$  (f) within cloud layer. The statistical metrics in the legends denote the mean and standard deviation values for all samples in three IOPs. The ACE-ENA summer, winter and SOCRATES are color-coded with pink, purple and green, respectively.

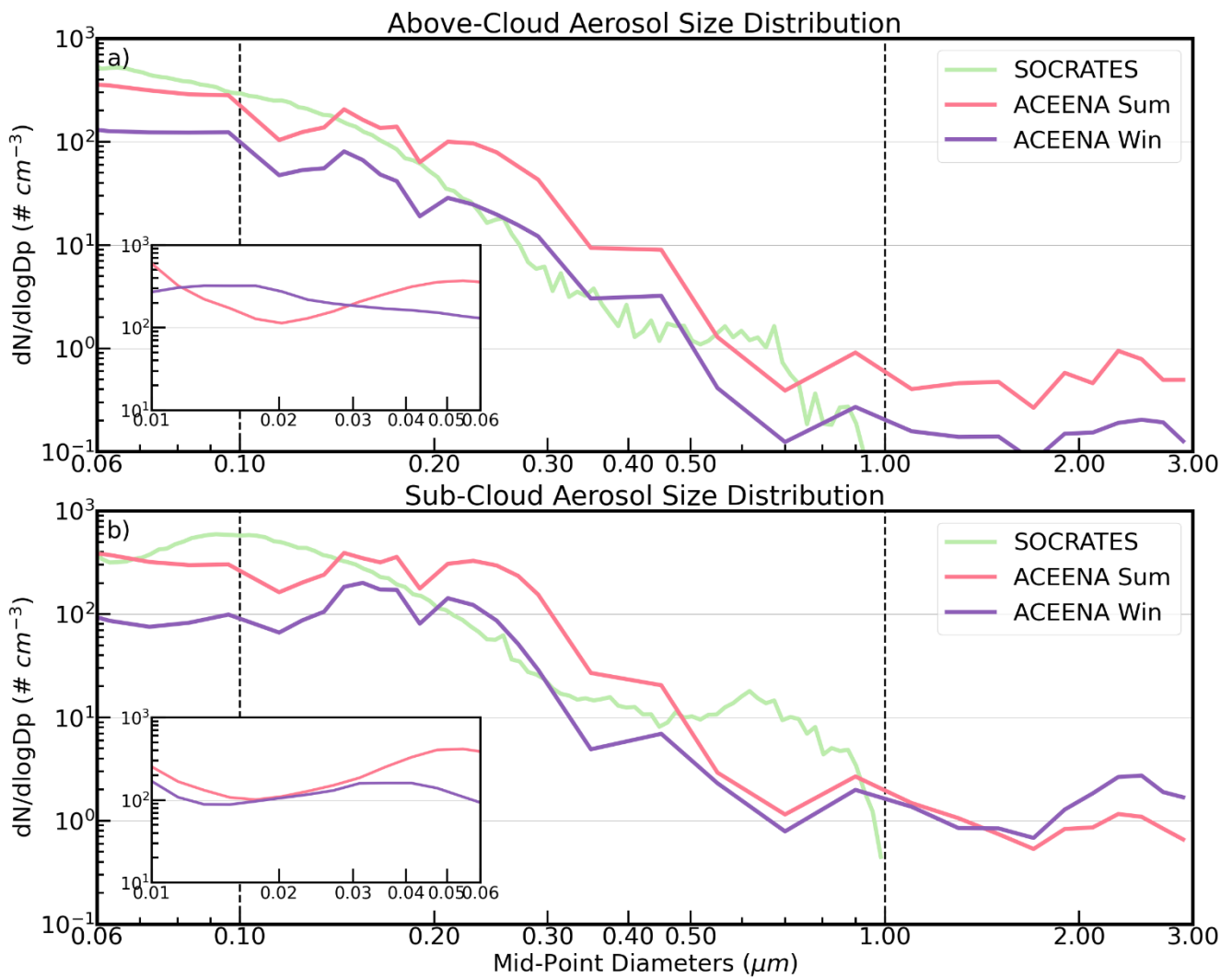
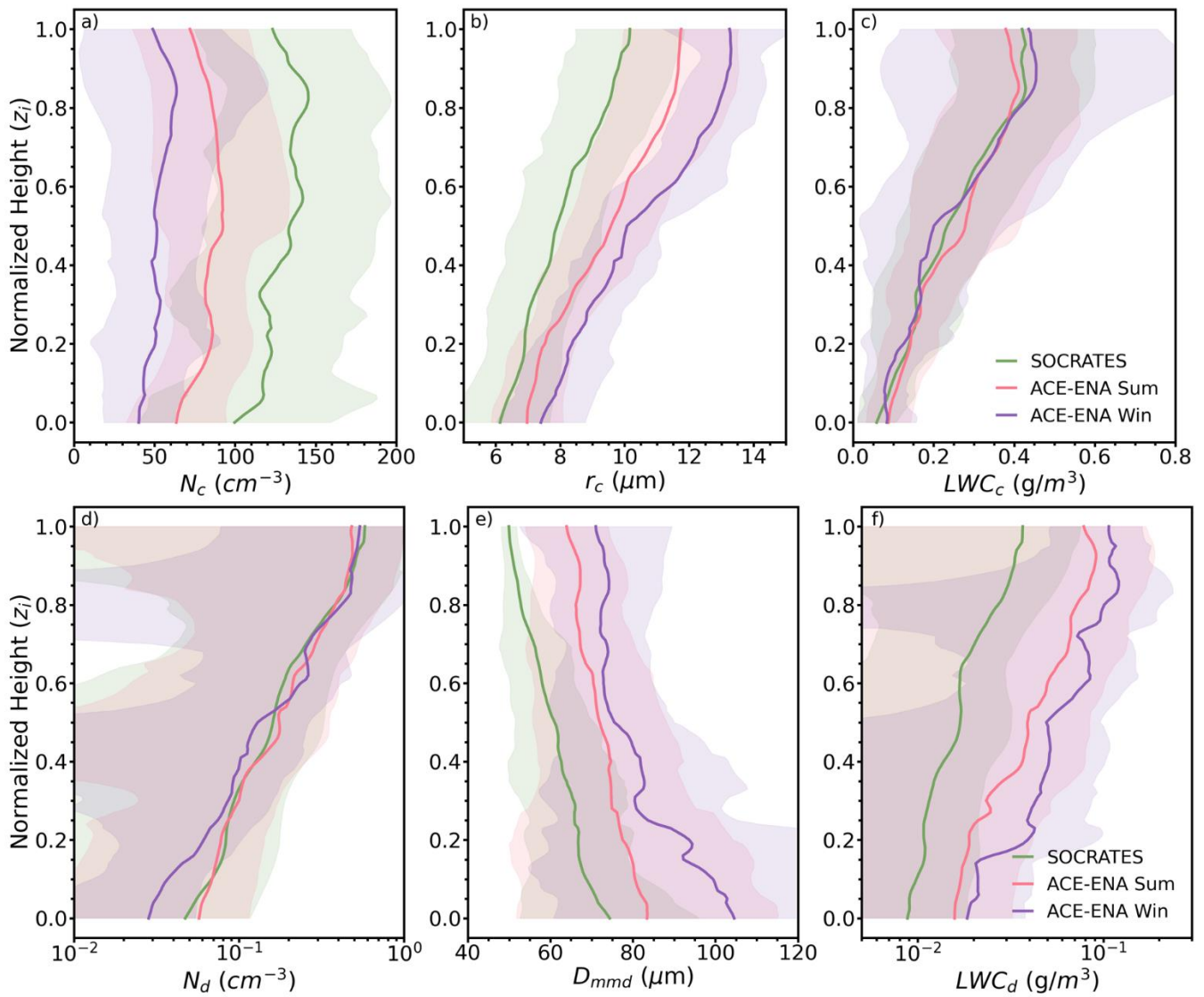
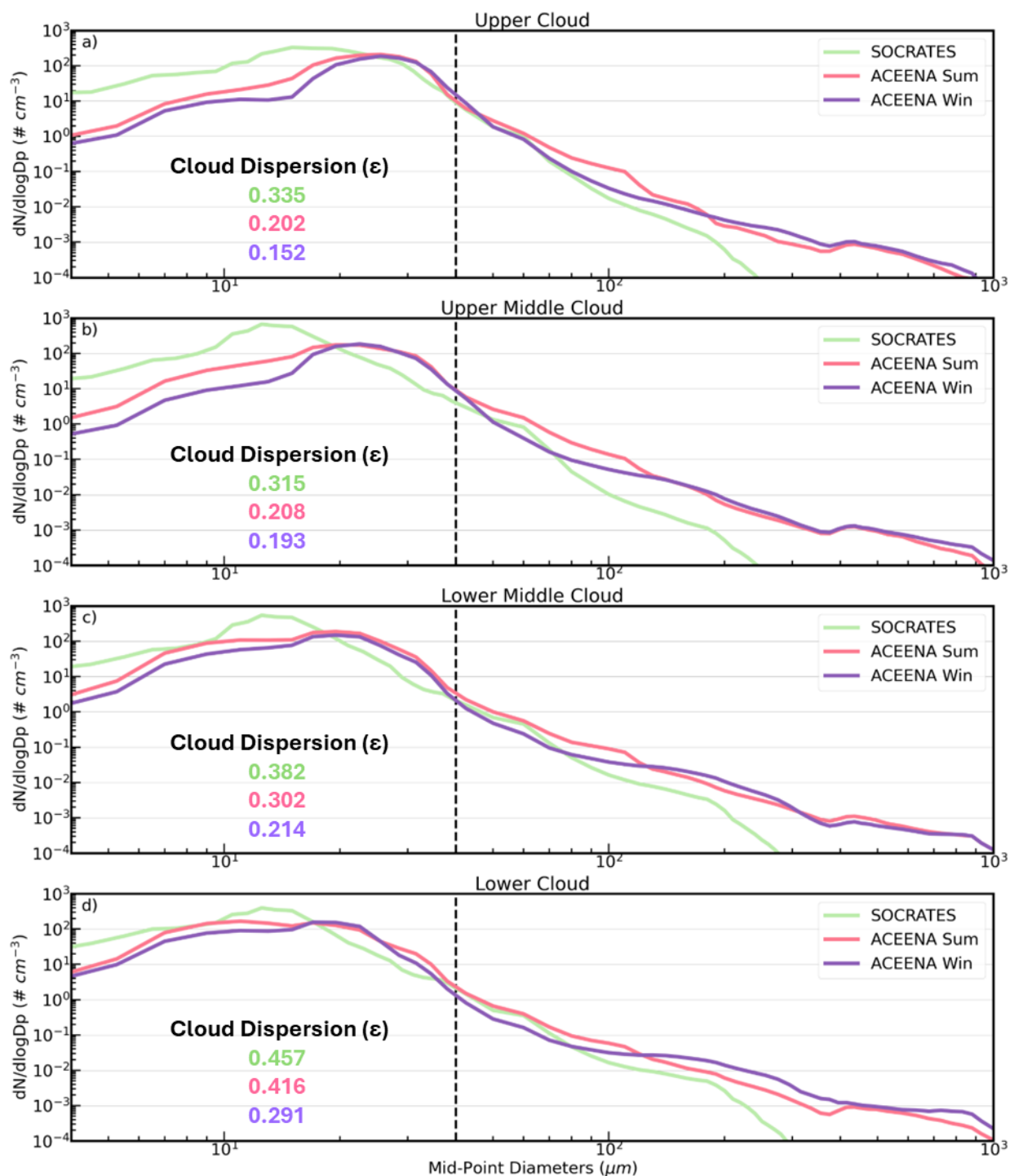


**Figure 2.** Aerosol size distributions ( $D_p = 0.06 - 3 \mu\text{m}$ ) for above-cloud (a) and sub-cloud (b) regimes. The vertical dashed line at  $D_p = 0.1 \mu\text{m}$  and at  $D_p = 1 \mu\text{m}$  denotes the demarcations between Accumulation mode, Aitken mode and Coarse mode aerosols. The inner plots denote a smaller range of Aitken mode size distribution ( $D_p = 0.01 - 0.06 \mu\text{m}$ ) available from ACE-ENA. The ACE-ENA summer, winter and SOCRATES are color-coded with pink, purple and green, respectively.



1222 **Figure 3.** Vertical distributions of  $N_c$  (a),  $r_c$  (b),  $LWC_c$  (c),  $N_d$  (d),  $D_{mmd}$  (e), and  $LWC_d$  (f). Here the  
 1223  $z_i = 0$  denotes cloud base and  $z_i = 1$  denotes cloud top. Shaded areas denote the inter-cloud-case  
 1224 standard deviations. The ACE-ENA summer, winter and SOCRATES are color-coded with pink, purple  
 1225 and green, respectively.



1226 **Figure 4.** Cloud and drizzle size distributions for a) upper cloud ( $z_i > 0.8$ ), b) upper-middle cloud ( $0.5 \leq$   
 1227  $z_i < 0.8$ ), c) lower-middle cloud ( $0.2 \leq z_i < 0.5$ ) and d) lower cloud ( $z_i < 0.2$ ). The vertical dashed  
 1228 line at  $D_p = 40 \mu\text{m}$  denotes the demarcation between cloud droplets and drizzle drops. The ACE-ENA  
 1229 summer, winter and SOCRATES are color-coded with pink, purple and green, respectively.

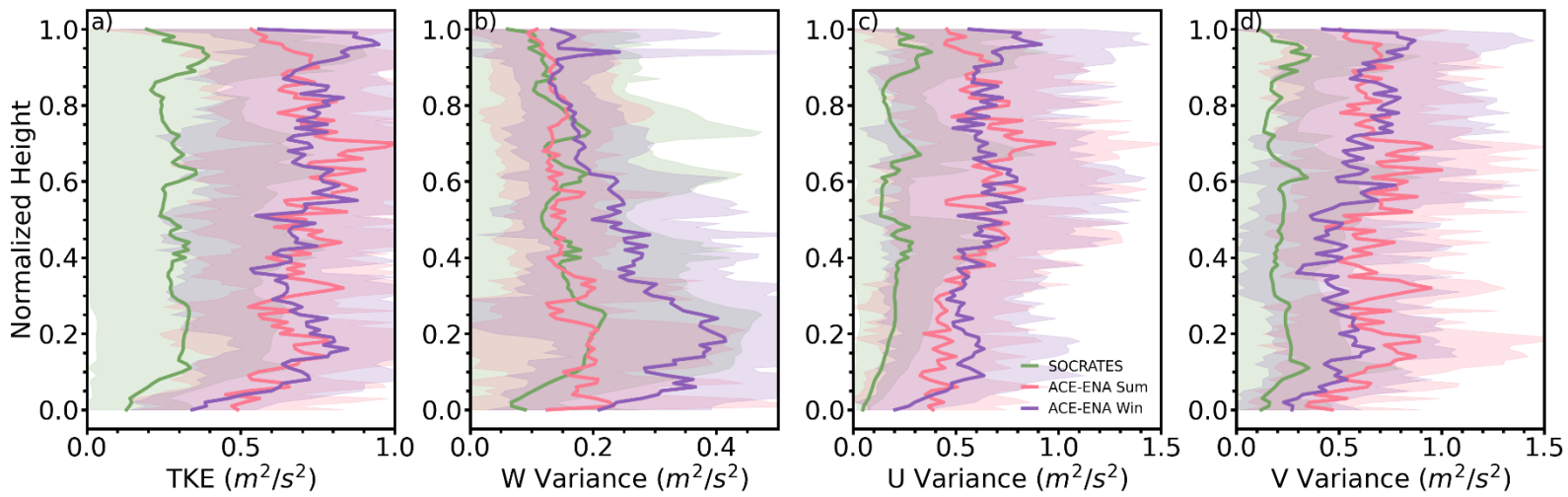


**Figure 5.** Vertical distributions of in-cloud  $TKE$  (a),  $w'^2$  (b),  $u'^2$  (c) and  $v'^2$  (d). Shaded areas denote the inter-cloud-case standard deviations. The ACE-ENA summer, winter and SOCRATES are color-coded with pink, purple and green, respectively.



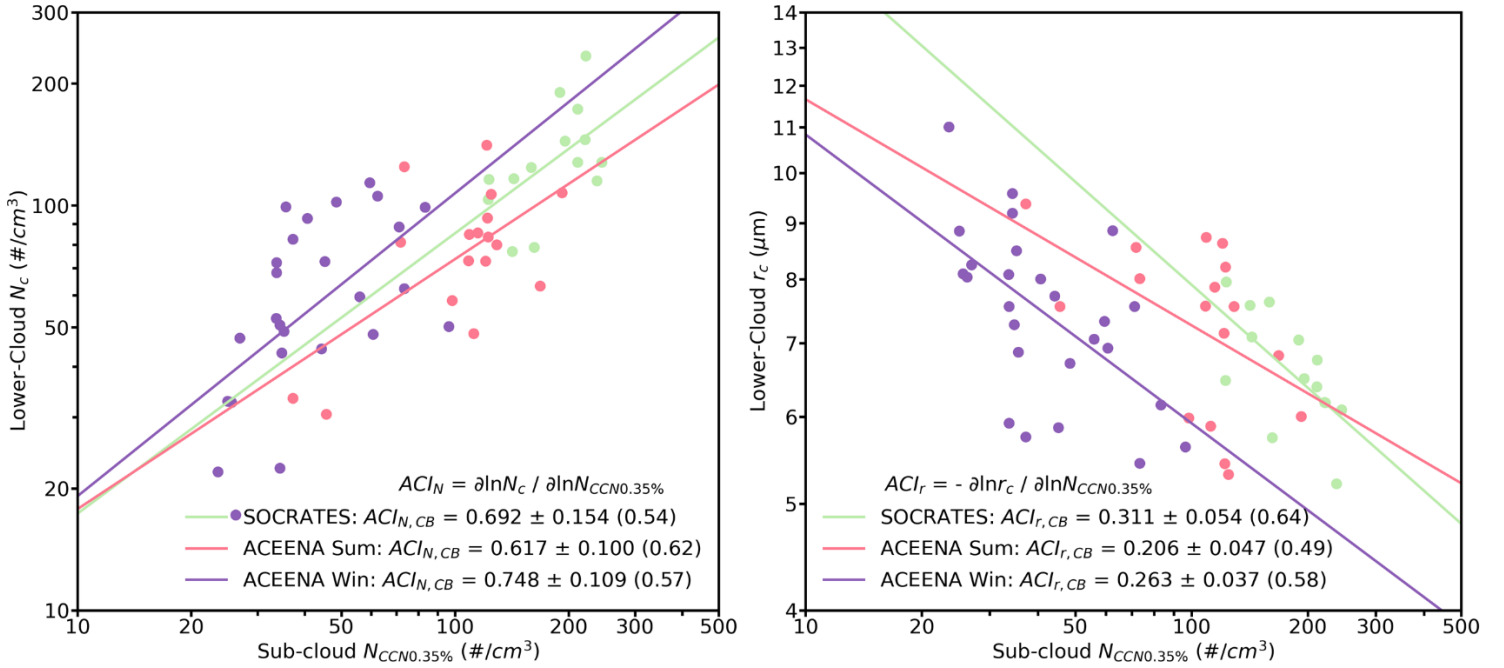


**Figure 6.** Scatterplots of the *a*)  $N_c$  and *b*)  $r_c$  at the lower-cloud ( $z_i < 0.2$ ) against the sub-cloud  $N_{CCN0.35\%}$ . The statistical metrics in the legends denote the ACI values and standard errors, and the absolute values of correlation coefficients (in parentheses). The ACE-ENA summer, winter and SOCRATES are color-coded with pink, purple and green, respectively.

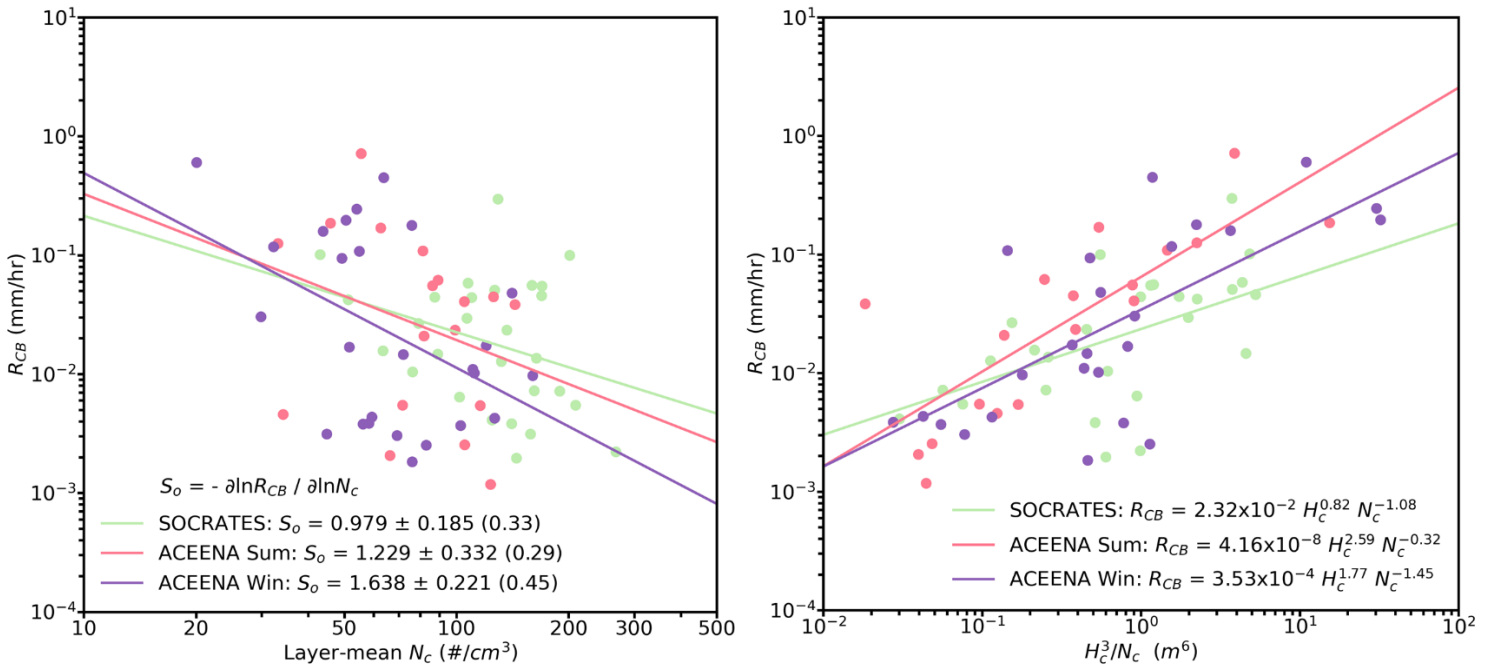


**Figure 7.** Scatterplots of the cloud base precipitation rate  $R_{CB}$  against the a) layer-mean  $N_c$  and b)  $H_c^3/N_c$ . ACE-ENA summer, winter and SOCRATES are color-coded with pink, purple and green, respectively.

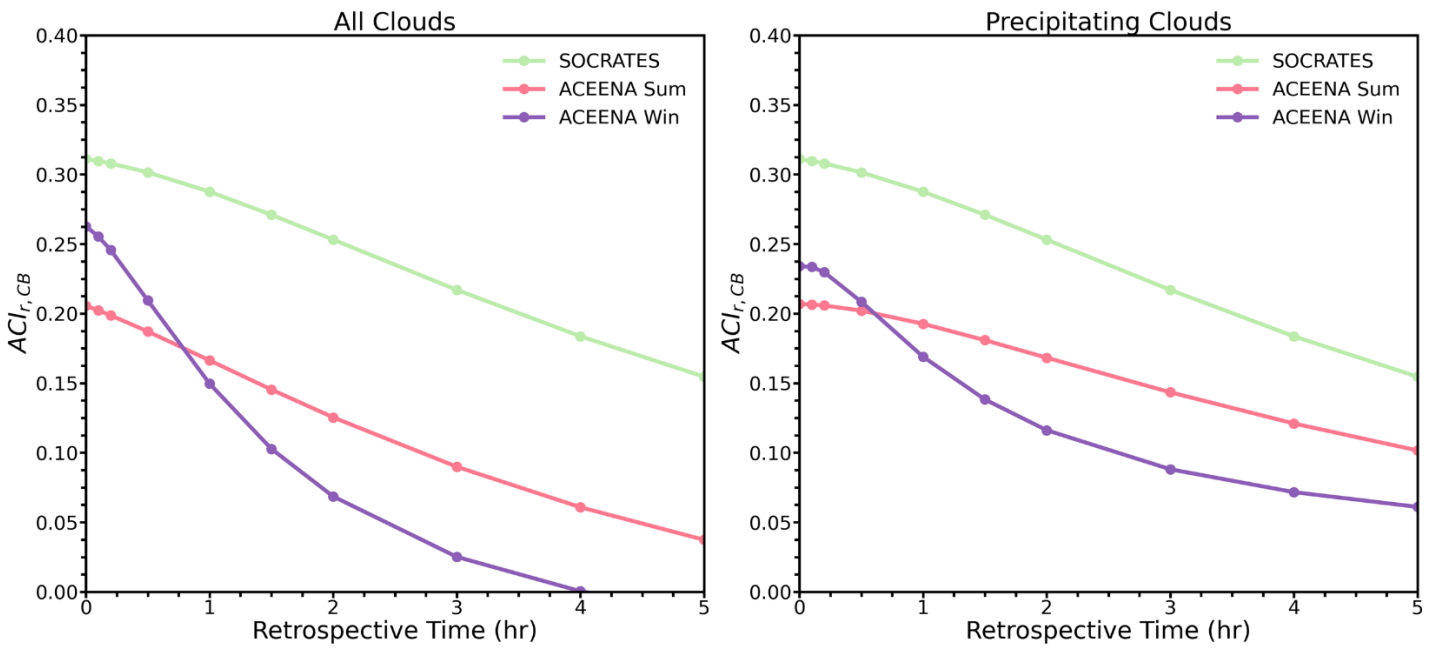


**Figure 8.**  $ACI_{r,CB}$  as a function of the sub-cloud  $N_{CCN0.35\%}$  retrospective time for a) all clouds and b) precipitating clouds.